J. Fluid Mech. (2022), *vol.* 934, A30, doi:10.1017/jfm.2021.1150

A physics-inspired alternative to spatial filtering for large-eddy simulations of turbulent flows

Perry L. Johnson†

Department of Mechanical and Aerospace Engineering, University of California, Irvine, CA, USA

(Received 6 June 2021; revised 11 October 2021; accepted 20 December 2021)

Large-eddy simulations (LES) are widely used for computing high Reynolds number turbulent flows. Spatial filtering theory for LES is not without its shortcomings, including how to define filtering for wall-bounded flows, commutation errors for non-uniform filters and extensibility to flows with additional complexity, such as multiphase flows. In this paper, the theory for LES is reimagined using a coarsening procedure that imitates nature. This physics-inspired coarsening approach is equivalent to Gaussian filtering for single-phase wall-free flows but opens up new insights for both physical understanding and modelling even in that simple case. For example, an alternative to the Germano identity is introduced and used to define a dynamic procedure without the need for a test filter. Non-uniform resolution can be represented in this framework without commutation errors, and the divergence-free condition is retained for incompressible flows. Potential extensions of the theory to more complex physics such as multiphase flows are briefly discussed.

Key words: turbulence modelling, turbulence simulation

1. Introduction

Because of the inherently multiscale nature of turbulence, the fine grids and small time steps required for direct numerical simulation (DNS) of turbulent flows are prohibitively expensive for many higher Reynolds number flow applications. Large-eddy simulation (LES) has become a popular technique for computing and predicting turbulent flows. In LES, the computational grid may be significantly coarser than the requirements of DNS, directly resolving only the large-scale features of the flow. Sub-grid models are introduced to approximate the net effect of unresolved fluctuations on the large-scale dynamics.

The theory for LES is based on reducing the number of computational degrees of freedom (DoFs) necessary for a digital representation of a turbulent flow, i.e. increasing the required grid spacing, typically using a low-pass spatial filter (Leonard 1975; Germano 1992; Sagaut 2006; Moser, Haering & Yalla 2021). The practical significance of spatial

† Email address for correspondence: perry.johnson@uci.edu

filtering theory for LES is not necessarily obvious, because most approaches assume an implicit filter. That is, an explicit calculation of a spatial filter is not necessary or even commonly employed in LES practice. What the theory of spatial filtering does provide is a definition of what the simulation aims to reproduce, and more importantly, a partial differential equation for the evolution of the resolved flow features, including a mathematical expression for the unclosed term(s) that need to be modelled. The definitions provided by spatial filtering enable the direct calculation of unclosed terms from DNS data, allowing for the *a priori* testing of candidate models (Borue & Orszag 1998) as well as the theoretical derivation or justification of many proposed models (Clark, Ferziger & Reynolds 1979; Bardina, Ferziger & Reynolds 1980; Verstappen 2011; Rozema *et al.* 2015). Perhaps the most notable fruit of spatial filtering theory for LES practice is the widely used dynamic procedure for determining model coefficients on the fly using an explicit test filter (Germano *et al.* 1991; Moin *et al.* 1991; Lilly 1992; Vreman, Geurts & Kuerten 1994; Meneveau, Lund & Cabot 1996; Bou-Zeid, Meneveau & Parlange 2005). Dynamic models are based on the Germano identity, which relates fields filtered at two different filter widths (Germano 1992).

However, spatial filtering LES theory is not without drawbacks, which have motivated some proposed modifications and alternative formulations. The optimal LES approach introduced by Langford & Moser (1999) addresses the inherent loss of information by invoking conditional averages and seeking a formulation for predicting single-time, multi-point statistics while minimizing short-time errors in general. Ultimately, it still relies on spatial filtering and assumes that no history information may be used for modelling, e.g. by Lagrangian averaging (Meneveau *et al.* 1996; Bou-Zeid *et al.* 2005) or evolving a sub-grid kinetic energy equation (Kim & Menon 1996).

The self-conditioned fields approach introduced by Fox (2003) and Pope (2010) redefines the objective of LES as the (unfiltered) velocity conditioned on the filtered velocity field (or another lower-dimensional representation). This conception of LES has many positive characteristics but makes direct (*a priori*) testing of models practically impossible. Self-conditioned fields LES also introduces additional closure terms pertaining to gradients with respect to conditioning variables (for which no models are proposed beyond ignoring the terms for expediency), and it largely does not provide much insight into how to construct models, mostly serving to justify existing models.

One significant difficulty with spatial filtering theory for LES is that non-uniform spatial filters do not commute with spatial differentiation, leading to commutation errors and loss of divergence-free velocity fields in the case of incompressible flows (Ghosal & Moin 1995; Langford & Moser 2001; Yalla *et al.* 2021). In practice, commutation errors are typically neglected and a divergence-free condition is imposed without justification. Another difficulty with spatial filtering arises close to a boundary, where the filter operator requires flow information from outside the fluid domain (Drivas & Nguyen 2018; Kumar, Quan & Eyink 2021), unless a non-uniform filter size is used (Bose & Moin 2014) leading to the commutation errors described above. The filtered field may also be conceived of as the solution to an elliptic partial differential equation (Germano 1986*a*,*b*; Bull & Jameson 2016), in which case the choice of boundary conditions may alleviate this particular difficulty (Bae & Lozano-Duran 2017). However, common LES treatments near the wall simply revert to techniques based on Reynolds averaged Navier–Stokes (RANS) without full justification in terms of spatial filtering. This is true for hybrid RANS–LES models (Piomelli & Balaras 2002; Frohlich & von Terzi 2008; Spalart 2009; Mockett, Fuchs & Thiele 2012) as well as wall-modelled LES (Larsson *et al.* 2016; Bose & Park 2018). The self-conditioned fields approach does manage to circumvent commutator errors altogether and to provide a well-defined near-wall behaviour matching the no-slip boundary condition

(Pope 2010), although these positive characteristics are counter-balanced by the challenges noted in the previous paragraph.

With interest growing in performing LES-like calculations with increasing physical complexity, spatial filtering theory is encountering more challenges. In multiphase flows, for instance, direct application of spatial filtering blurs the interface (Labourasse *et al.* 2007), unnecessarily losing its distinctiveness even though sharp interface methods exist for careful, robust treatment such discontinuities. It is desirable to have an LES theory that allows for retaining sharp interfaces while removing features such as small-scale ripples that cannot be resolved on a coarse grid (Tryggvason & Lu 2020). One alternative is the dual-scale approach of Herrmann (2013), but this requires DNS-like resolution for the phase indicator field (or volume fraction field) and a super-resolution enrichment for the velocity (Herrmann, Kedelty & Ziegenhein 2018).

In the simulation of turbulent flows laden with small particles, including unresolved droplets or bubbles in multiphase flows, it is common to avoid the need to resolve the flow around a particle (i.e. computationally resolve the proper boundary or interface conditions at the particle surface) using a Lagrangian tracking approach. A closure such as a drag law must be introduced. When the particle is much smaller than the Kolmogorov scale, the Reynolds number based on its relative velocity is small, and the particle is not near a flow boundary, the Lagrangian tracking approach can be quite precise (Maxey & Riley 1983; Balachandar & Eaton 2010). In other more complex scenarios, Lagrangian tracking represents an approximate treatment motivated by computational tractability not unlike spatial filtering for LES. In fact, if the goal of reducing computational DoF is indeed central to LES, then the mathematical theory of LES should be fundamentally compatible with an Eulerian–Lagrangian approach to particle-laden flows in a way that spatial filtering is not. This includes potential hybrid approaches to multiphase flows that combine the direct resolution of large-scale interface features with a Lagrangian tracking approach for small-scale features (Kim & Moin 2020).

While LES may be practiced in isolation from specific concerns of a consistent framework, a specific definition of that which an LES aspires to accurately reproduce is required for advanced techniques such as data-driven closure (Sarghini, de Felice & Santini 2003; Moreau, Teytaud & Bertoglio 2006; Gamahara & Hattori 2017; Vollant, Balarac & Corre 2017; Wang *et al.* 2018; Beck, Flad & Munz 2019; Cheng *et al.* 2019; Yang *et al.* 2019; Zhou *et al.* 2019; Sirignano, MacArt & Freund 2020; Xie, Wang & Weinan 2020*a*; Xie, Yuan & Wang 2020*b*; Yuan, Xie & Wang 2020; Bode *et al.* 2021; Duraisamy 2021; Freund & Ferrante 2021; Park & Choi 2021; Portwood *et al.* 2021; Prakash, Jansen & Evans 2021; Stoffer *et al.* 2021; Wang *et al.* 2021) and super-resolution enrichment (Domaradzki & Loh 1999; Scotti & Meneveau 1999; Stolz & Adams 1999; Milano & Koumoutsakos 2002; Leonard 2016; Ghate & Lele 2017; Maulik & San 2017; Bassenne *et al.* 2019; Wang, Zhao & Ihme 2019; Ghate & Lele 2020; Liu *et al.* 2020; Kim *et al.* 2021). For example, without a clear definition of what an LES solution should represent, one cannot train a neural network to serve as a sub-grid closure in a robust way. In this sense, the particular relationship between an LES solution and the fully resolved flow must be afforded more direct attention in the age of data. This is especially true for more complex scenarios with solid boundaries, interfaces and multiphysics; where pure spatial filtering is not likely the optimal approach.

The scope of this paper is as follows. This paper introduces the concept of physics-inspired coarsening (PIC) as a proposed alternative to spatial filtering as a basis for LES. In addition to laying the groundwork of PIC theory, results for the simplest of turbulent flows are demonstrated with *a priori* and *a posteriori* testing of representative PIC-based models. Beyond that, the paper explores the extensibility of PIC theory for

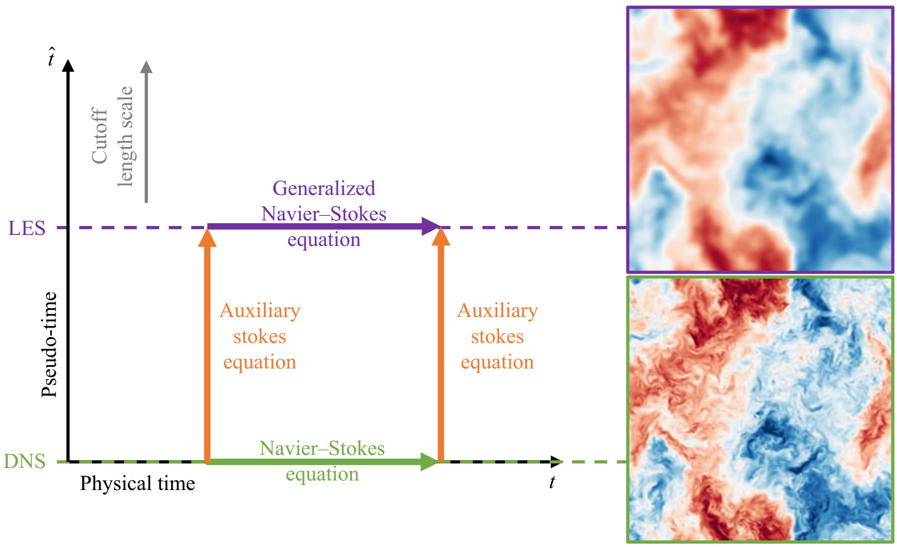

Figure 1. PIC for LES defines a generalized velocity field as a function of physical time (t) and pseudo-time ($\hat{t} \sim$ grid-size^2). The generalized Navier–Stokes equation for the LES velocity in physical time requires a closure model.

complex flows to motivate future work in various directions. The basic theory of PIC is established in § 2. Following that, § 3 explores in detail single-phase unbounded flows with uniform resolution, for which PIC is equivalent to Gaussian filtering. Even with this equivalence, PIC theory provides new insights into energy cascade physics and model development. Preliminary models based on these insights are demonstrated with *a priori* and *a posteriori* testing. In § 4, PIC theory is expanded to include a number of more complex effects such as anisotropic and non-uniform resolution, heat and mass transfer and flows with solid boundaries and multiphase interfaces. Conclusions are drawn in § 5.

2. Physics-inspired coarsening

The underlying philosophy of PIC is to view the removal of DoFs from a flow more as an imitation of nature than as an image processing trick. As a primary example, the viscosity, μ, provides a natural mechanism that prevents the creation of motions smaller than the Kolmogorov microscale, $\eta = \nu^{3/4}\epsilon^{-1/4}$, where $\nu = \mu/\rho$ is the kinematic viscosity, ρ is the fluid mass density and ϵ is the turbulent dissipation rate. This natural mechanism may be imitated for LES theory by conjuring an artificial viscous process to further smooth a frozen snapshot of turbulence, removing small motions below a cutoff length scale, $\ell > \eta$. The artificial physics-inspired process evolves in a pseudo-time that is independent of physical time. The overall idea of PIC is illustrated in figure 1 and described in detail in the remainder of this section. The final subsection then reviews the spatial filtering theory of LES for comparison and contrast.

2.1. *Navier–Stokes equation*

For the present purposes, an incompressible flow of a Newtonian fluid is considered. A velocity vector field, $\boldsymbol{u} = \boldsymbol{u}(\boldsymbol{x}, t)$, evolves as a function of space, $\boldsymbol{x}$, and time, t, according to the Navier–Stokes equation

$$\frac{\partial u_i}{\partial t} + \frac{\partial}{\partial x_j}\left[u_i u_j + p\delta_{ij} - \nu\left(\frac{\partial u_i}{\partial x_j} + \frac{\partial u_j}{\partial x_i}\right)\right] = 0, \quad \frac{\partial u_j}{\partial x_j} = 0. \tag{2.1}$$

The pressure (divided by density), $p(\boldsymbol{x}, t)$, enforces the divergence-free condition. A Poisson equation for the pressure follows from the divergence of the Navier–Stokes equation

$$\nabla^2 p = -\frac{\partial u_i}{\partial x_j}\frac{\partial u_j}{\partial x_i}. \tag{2.2}$$

Thus, a fully resolved simulation (DNS) evolves (2.1) together with (2.2) in physical time with pseudo-time fixed at zero, $\hat{t} = 0$, indicated by the green arrow in figure 1.

2.2. *Auxiliary Stokes equation*

For the physics-inspired approach, a generalized velocity field, $\boldsymbol{w} = \boldsymbol{w}(\boldsymbol{x}, t; \hat{t})$, is defined as a function of both time, t, and a pseudo-time, $\hat{t}$. The generalized velocity field at $\hat{t} = 0$ corresponds to the physical velocity field

$$\boldsymbol{w}(\boldsymbol{x}, t; 0) = \boldsymbol{u}(\boldsymbol{x}, t). \tag{2.3}$$

As $\hat{t}$ increases, small-scale motions are removed from the generalized velocity field. Thus, the pseudo-time is an indicator of the resolution length scale of the generalized velocity. To accomplish this, an auxiliary Stokes equation may be introduced to govern the pseudo-time evolution

$$\frac{\partial w_i}{\partial \hat{t}} + \frac{\partial}{\partial x_j}\left[\hat{p}\delta_{ij} - \hat{\nu}\left(\frac{\partial w_i}{\partial x_j} + \frac{\partial w_j}{\partial x_i}\right)\right] = 0, \quad \frac{\partial w_j}{\partial x_j} = 0. \tag{2.4}$$

The nonlinear term of the Navier–Stokes equation ($u_i u_j$) is removed for (2.4), so there is no energy cascade in pseudo-time and hence no resupply of energy to small scales dissipated by pseudo-viscosity, $\hat{\nu}(\boldsymbol{x})$. The length scale at which the flow is smoothed may be heuristically estimated as $\ell \sim \sqrt{\hat{\nu}\hat{t}}$. A pseudo-pressure, $\hat{p}(\boldsymbol{x}, t; \hat{t})$, is also introduced to enforce a divergence-free condition for the generalized velocity at all pseudo-times. The divergence of the auxiliary Stokes equation is a Poisson equation for the pseudo-pressure

$$\nabla^2 \hat{p} = \frac{\partial^2}{\partial x_i \partial x_j}\left[\hat{\nu}\left(\frac{\partial w_i}{\partial x_j} + \frac{\partial w_j}{\partial x_i}\right)\right]. \tag{2.5}$$

Thus, a DNS may be artificially coarsened by, instead of applying a spatial filter, advancing (2.4) in pseudo-time together with (2.5) having initial conditions set by (2.3). This is represented in figure 1 by the orange arrows. In the case of a moving reference frame, the coordinate system only advances in physical time. It is frozen in pseudo-time by definition, so that Galilean invariance is satisfied. Note that the pseudo-viscosity is distinct from the idea of an eddy viscosity (or turbulent viscosity) often used to model turbulent flows. The pseudo-viscosity acts only in pseudo-time and simply enables the coarsening procedure that is an alternative to spatial filtering. An eddy viscosity acts in physical time and attempts to approximate the evolution of a coarsened velocity field in physical time, which is considered next.

2.3. *Generalized Navier–Stokes equation*

Explicit filtering is not typically used in practice for LES. Similarly, it is not envisioned at present that PIC-based LES practice will (necessarily) include the numerical solution of an auxiliary Stokes equation. The significance of (2.4), rather, is its implication for the evolution of the generalized velocity in physical time, keeping $\hat{t} \sim \ell^2$ fixed based on the grid resolution. This is illustrated by the purple arrow in figure 1 and corresponds to establishing the effective equations for solving a coarsened representation of the flow, which may in practice be done on a coarser grid.

The outcome of the auxiliary Stokes equation ensures that the Navier–Stokes equation must be altered to accurately describe the evolution of the coarsened flow field in physical time. Thus, an effective evolution equation for LES may be derived by finding the appropriate residual force, $\boldsymbol{F}$, such that

$$\frac{\partial w_i}{\partial t} + \frac{\partial}{\partial x_j}\left[w_i w_j + \phi\delta_{ij} - \nu\left(\frac{\partial w_i}{\partial x_j} + \frac{\partial w_j}{\partial x_i}\right)\right] = F_i, \quad \frac{\partial w_j}{\partial x_j} = 0. \tag{2.6}$$

When $\hat{t} = 0$, the generalized velocity does satisfy (2.1) because of the initial condition, (2.3). This means that, $\boldsymbol{F}(\boldsymbol{x}, t; 0) = 0$.

Because the auxiliary Stokes equation globally conserves momentum in the absence of fluxes through domain boundaries, the residual force must likewise conserve momentum, and it may be written as the divergence of a residual stress tensor

$$F_i = \frac{\partial \sigma_{ij}}{\partial x_j}. \tag{2.7}$$

Thus, the evolution of the generalized velocity in physical time is given by the generalized Navier–Stokes equation

$$\frac{\partial w_i}{\partial t} + \frac{\partial}{\partial x_j}\left[w_i w_j + \sigma_{ij} + \phi\delta_{ij} - \nu\left(\frac{\partial w_i}{\partial x_j} + \frac{\partial w_j}{\partial x_i}\right)\right] = 0, \quad \frac{\partial w_j}{\partial x_j} = 0. \tag{2.8}$$

Note that the divergence-free constraint on the auxiliary Stokes equation implies a divergence-free condition for the physical time evolution as well. This is enforced by a generalized pressure, $\phi(\boldsymbol{x}, t; \hat{t})$, that is distinct from the pseudo-pressure, $\hat{p}$, which acts only during pseudo-time evolution. The generalized pressure may be found by solution of the following Poisson equation:

$$\nabla^2\phi = -\frac{\partial w_i}{\partial x_j}\frac{\partial w_j}{\partial x_i} - \frac{\partial^2 \sigma_{ij}}{\partial x_i \partial x_j}. \tag{2.9}$$

Equation (2.8), together with (2.9) is unclosed in general. The residual stress tensor field must be approximated in terms of the generalized velocity field in order to solve for its evolution. More specifically, only the deviatoric component of $\boldsymbol{\sigma}$ is material to the closure problem, because any isotropic component may be lumped in with the generalized pressure and found via (2.9). For consistency, it is required that the generalized velocity, $\boldsymbol{w}$, evolves according to the Navier–Stokes equation for $\hat{t} = 0$. That is, (2.8) must be identical to (2.1) when $\hat{t} = 0$. Thus

$$\phi(\boldsymbol{x}, t; 0) = p(\boldsymbol{x}, t), \quad \sigma_{ij}(\boldsymbol{x}, t; 0) = 0. \tag{2.10a,b}$$

2.4. *Residual stress tensor equation*

The significance of the above theory is its implications for the mathematical definition of the residual stress tensor, which is found by requiring consistency between the pseudo-time and physical time evolution of the generalized velocity field sketched in figure 1. Specifically, $\boldsymbol{\sigma}$ may be defined by asserting that advancing the generalized velocity field from $(t_0, \hat{t}_0)$ to $(t_f, \hat{t}_f)$ must be independent of the path in t–$\hat{t}$ space. Breaking the evolution in t–$\hat{t}$ space into infinitesimal increments, this requirement may be written as

$$\frac{\partial}{\partial \hat{t}}\left(\frac{\partial w_i}{\partial t}\right) = \frac{\partial}{\partial t}\left(\frac{\partial w_i}{\partial \hat{t}}\right), \tag{2.11}$$

which is simply the symmetry of mixed partial derivatives. More detailed treatment of the implications of this constraint for the form of the residual stress tensor will be given later.

2.5. *Kinetic energy equations*

The scale-wise dynamics of kinetic energy is crucial to the representation of turbulent flows. The generalized kinetic energy (per unit mass) in PIC is given by $\frac{1}{2}w_i w_i$. First, consider how kinetic energy evolves in pseudo-time. Multiplying the auxiliary Stokes equation, (2.4), by w_i and using a product rule on the viscous term

$$\frac{\partial(\frac{1}{2}w_i w_i)}{\partial \hat{t}} + \frac{\partial}{\partial x_j}[\hat{p} w_j - 2\hat{\nu} w_i S_{ij}] = -2\hat{\nu} S_{ij} S_{ij}, \tag{2.12}$$

where $S_{ij} = \frac{1}{2}(\partial w_i/\partial x_j + \partial w_j/\partial x_i)$ is the generalized strain-rate tensor. As pseudo-time increases, kinetic energy is removed by the pseudo-viscosity at a rate $2\hat{\nu} S_{ij} S_{ij} \geq 0$.

The dynamics of generalized kinetic energy in physical time (at fixed, finite pseudo-time) can be written by multiplying the generalized Navier–Stokes equation, (2.8) by w_i

$$\frac{\partial(\frac{1}{2}w_i w_i)}{\partial t} + \frac{\partial}{\partial x_j}\left[\frac{1}{2}w_i w_i w_j + w_i \sigma_{ij} + \phi w_j - 2\nu w_i S_{ij}\right] = \sigma_{ij} S_{ij} - 2\nu S_{ij} S_{ij}. \tag{2.13}$$

In addition to direct viscous dissipation, $2\nu S_{ij} S_{ij} \geq 0$, the generalized kinetic energy is removed at a rate $\varPi = -\sigma_{ij} S_{ij}$. Note that $\varPi$ may be positive or negative in general, but that the expectation for turbulence dynamics is a preference toward $\varPi > 0$ representing the kinetic energy cascade. That is, $\varPi$ represents the rate at which kinetic energy associated with motions larger than $\ell \sim \sqrt{\hat{\nu}\hat{t}}$ is passed to motions smaller than ℓ. Thus, an important consideration for any closure model for σ_{ij} is its ability to remove energy at the proper rate to mimic the energy cascade.

2.6. *Juxtaposition with spatial filtering*

The traditional approach to LES theory is based on developing equations for the filtered velocity field (Leonard 1975; Germano 1992)

$$\bar{u}_i^{\ell}(\boldsymbol{x}, t) = \iiint G^{\ell}(\boldsymbol{r}) u_i(\boldsymbol{x} + \boldsymbol{r}, t)\, \mathrm{d}\boldsymbol{r}, \quad \mathcal{F}\{\bar{u}_i^{\ell}\} = (2\pi)^3 \mathcal{F}\{G^{\ell}\}\mathcal{F}\{u_i\}. \tag{2.14a,b}$$

The relative width of the filter is ℓ, with larger values of ℓ resulting in coarser fields. The notation $\mathcal{F}$ is used for a Fourier transform in three dimensions. The definition used here for an arbitrary field a is

$$\mathcal{F}\{a\}(\boldsymbol{k}) = \frac{1}{(2\pi)^3} \iiint a(\boldsymbol{x}) \exp(-\mathrm{i}\boldsymbol{k}\cdot\boldsymbol{x})\,\mathrm{d}\boldsymbol{x}. \tag{2.15}$$

The three-dimensional inverse Fourier transform for an arbitrary function b is therefore

$$\mathcal{F}^{-1}\{b\}(\boldsymbol{x}) = \iiint b(\boldsymbol{k}) \exp(\mathrm{i}\boldsymbol{k}\cdot\boldsymbol{x})\,\mathrm{d}\boldsymbol{k}. \tag{2.16}$$

This Fourier transform definition is commonly used for turbulence theory, e.g. (Tennekes & Lumley 1972; Monin & Yaglom 1975; Pope 2000).

LES practitioners rarely rely on a specific filter kernel shape. Common filter shapes used for theoretical appraisals include top-hat, spectral cutoff and Gaussian kernels (Borue & Orszag 1998). For example, the Gaussian filter kernel is given by

$$G^\ell(\boldsymbol{r}) = \frac{1}{(2\pi\ell)^{3/2}} \exp\left(-\frac{|\boldsymbol{r}|^2}{2\ell^2}\right), \quad (2\pi)^3\mathcal{F}\{G^\ell\}(\boldsymbol{k}) = \exp\left(-\frac{1}{2}|\boldsymbol{k}|^2\ell^2\right). \tag{2.17a,b}$$

The Gaussian filter provides a balanced trade-off between localization in physical space and wavenumber space, with exponential-of-square dropoff in both.

For a more general class of filter shapes, the Navier–Stokes equation, (2.1), may be filtered to yield an equation for the filtered velocity field

$$\frac{\partial \bar{u}_i^\ell}{\partial t} + \frac{\partial}{\partial x_j}\left[\bar{u}_i^\ell \bar{u}_j^\ell + \tau_{ij}^\ell + \bar{p}^\ell \delta_{ij} - \nu\left(\frac{\partial \bar{u}_i^\ell}{\partial x_j} + \frac{\partial \bar{u}_j^\ell}{\partial x_i}\right)\right] = \mathcal{C}_i, \quad \frac{\partial \bar{u}_j^\ell}{\partial x_j} = \mathcal{D}. \tag{2.18a,b}$$

Here, the subfilter stress tensor, $\tau_{ij}^\ell = \overline{u_i u_j}^\ell - \bar{u}_i^\ell \bar{u}_j^\ell$, plays a role analogous to that of the residual stress tensor in PIC, σ_{ij}, although their mathematical definitions may differ. Also, the filtered pressure, $\bar{p}^\ell$, is analogous to the generalized pressure in PIC, ϕ.

The vector $\boldsymbol{\mathcal{C}}$ and scalar $\mathcal{D}$ in (2.18a,b) represent commutator terms that are zero if the filtering operation is spatially uniform, i.e. $\ell \neq \ell(\boldsymbol{x})$. In the case of spatially varying filter width, these commutator errors arise and (theoretically) require additional treatment for LES modelling (Ghosal & Moin 1995; Langford & Moser 2001; Moser *et al.* 2021; Yalla *et al.* 2021).

The kinetic energy of the filtered velocity field evolves as

$$\frac{\partial(\frac{1}{2}\bar{u}_i^\ell \bar{u}_i^\ell)}{\partial t} + \frac{\partial}{\partial x_j}\left[\frac{1}{2}\bar{u}_i^\ell \bar{u}_i^\ell \bar{u}_j^\ell + \bar{u}_i \tau_{ij}^\ell + \bar{p}^\ell \bar{u}_j^\ell - 2\nu \bar{u}_i^\ell \bar{s}_{ij}^\ell\right] = \tau_{ij}^\ell \bar{s}_{ij}^\ell - 2\nu \bar{s}_{ij}^\ell \bar{s}_{ij}^\ell. \tag{2.19}$$

The strain-rate tensor is $s_{ij} = \frac{1}{2}(\partial u_i/\partial x_j + \partial u_j/\partial x_i)$ and the filtered strain-rate tensor is $\bar{s}_{ij}^\ell = \frac{1}{2}(\partial \bar{u}_i^\ell/\partial x_j + \partial \bar{u}_j^\ell/\partial x_i)$. The two sinks of the filtered kinetic energy are analogous to those of the generalized kinetic energy in (2.13).

The above derivation presumed an unbounded domain in the filter definition. Section 3 explores the similarity between PIC and filtering in the context of unbounded flows with uniform resolution. Even in this case, PIC provides useful insight. Then, § 4 shows how PIC may be extended to more complex flows, including those which represent a challenge to the spatial filtering approach to LES theory.

3. Unbounded flows with uniform resolution

3.1. *Equivalence of PIC with Gaussian filtering*

For unbounded flows with uniform resolution (uniform $\hat{\nu}$), the pseudo-pressure satisfies a Laplace equation in free space, so $\hat{p} = 0$. That is, the pseudo-pressure is not needed to enforce the divergence-free condition on the generalized velocity. In this case, the auxiliary Stokes equation simplifies to

$$\frac{\partial w_i}{\partial \hat{t}} = \hat{\nu}\nabla^2 w_i, \quad w_i(\boldsymbol{x}, t; 0) = u_i(\boldsymbol{x}, t). \tag{3.1a,b}$$

The formal solution to (3.1*a*,*b*) in an unbounded domain is readily obtained

$$w_i(\boldsymbol{x}, t; \hat{t}) = \iiint \frac{1}{(4\pi\hat{\nu}\hat{t})^{3/2}} \exp\left(-\frac{|\boldsymbol{r}|^2}{4\hat{\nu}\hat{t}}\right) u_i(\boldsymbol{x}+\boldsymbol{r}, t)\, \mathrm{d}\boldsymbol{r} \equiv \bar{u}_i^{\ell}(\boldsymbol{x}, t), \tag{3.2}$$

which is precisely a Gaussian filter with width $\ell = \sqrt{2\hat{\nu}\hat{t}}$. Therefore, the PIC approach is precisely equivalent to spatial filtering with a Gaussian kernel for unbounded flows with uniform resolution. All the strengths and theoretical insights of spatial filtering naturally carry over, but a new perspective on the residual stress tensor also emerges.

3.2. *PIC expression for the residual stress tensor*

With the equivalence to Gaussian filtering established for PIC of unbounded flows with uniform resolution, the mathematical definition of the residual stress tensor could be straightforwardly written as $\sigma_{ij} = \tau_{ij} \equiv \overline{u_i u_j}^{\ell} - \bar{u}_i^{\ell}\bar{u}_j^{\ell}$. However, insights beyond those arrived at via spatial filtering may be obtained by following the PIC logic further in the form of (2.11).

In the following, flow subjected to an arbitrary (divergence-free) forcing function, $\boldsymbol{f}(\boldsymbol{x}, t)$ is considered, so (2.1) becomes

$$\frac{\partial u_i}{\partial t} + \frac{\partial}{\partial x_j}\left[u_i u_j + p\delta_{ij} - \nu\left(\frac{\partial u_i}{\partial x_j} + \frac{\partial u_j}{\partial x_i}\right)\right] = f_i, \quad \frac{\partial u_j}{\partial x_j} = 0. \tag{3.3}$$

The generalized Navier–Stokes equations are likewise supplemented with a generalized force, $\boldsymbol{g}(\boldsymbol{x}, t)$, that represents the impact of the physical forcing on the coarsened flow representation

$$\frac{\partial w_i}{\partial t} + \frac{\partial}{\partial x_j}\left[w_i w_j + \sigma_{ij} + \phi\delta_{ij} - \nu\left(\frac{\partial w_i}{\partial x_j} + \frac{\partial w_j}{\partial x_i}\right)\right] = g_i, \quad \frac{\partial w_j}{\partial x_j} = 0. \tag{3.4}$$

Substituting equations (3.1*a*) and (3.4) into (2.11)

$$\frac{\partial}{\partial \hat{t}}\left(\nu\nabla^2 w_i - \frac{\partial \phi}{\partial x_i} - \frac{\partial w_i w_j}{\partial x_j} - \frac{\partial \sigma_{ij}}{\partial x_j} + g_i\right) - \frac{\partial}{\partial t}(\hat{\nu}\nabla^2 w_i) = 0, \tag{3.5}$$

and rearranging in terms of time and pseudo-time derivatives,

$$\nu\nabla^2\left(\frac{\partial w_i}{\partial \hat{t}}\right) - \frac{\partial}{\partial x_i}\left(\frac{\partial \phi}{\partial \hat{t}}\right) - \frac{\partial}{\partial x_j}\left(w_i\frac{\partial w_j}{\partial \hat{t}} + w_j\frac{\partial w_i}{\partial \hat{t}}\right) - \frac{\partial}{\partial x_j}\left(\frac{\partial \sigma_{ij}}{\partial \hat{t}}\right) + \frac{\partial g_i}{\partial \hat{t}} = \hat{\nu}\nabla^2\left(\frac{\partial w_i}{\partial t}\right), \tag{3.6}$$

and further substitution of (3.1*a*) and (3.4)

$$\nu\nabla^2(\hat{\nu}\nabla^2 w_i) - \frac{\partial}{\partial x_i}\left(\frac{\partial\phi}{\partial\hat{t}}\right) - \frac{\partial}{\partial x_j}(\hat{\nu}w_i\nabla^2 w_j + \hat{\nu}w_j\nabla^2 w_i) - \frac{\partial}{\partial x_j}\left(\frac{\partial\sigma_{ij}}{\partial\hat{t}}\right) + \frac{\partial g_i}{\partial\hat{t}}$$
$$= \hat{\nu}\nabla^2\left(\nu\nabla^2 w_i - \frac{\partial\phi}{\partial x_i} - \frac{\partial w_i w_j}{\partial x_j} - \frac{\partial\sigma_{ij}}{\partial x_j} + g_i\right). \tag{3.7}$$

Now, further simplification leads to

$$-\frac{\partial}{\partial x_j}\left(\frac{\partial\sigma_{ij}}{\partial\hat{t}} - \hat{\nu}\nabla^2\sigma_{ij} - 2\hat{\nu}\frac{\partial w_i}{\partial x_k}\frac{\partial w_j}{\partial x_k} + \frac{\partial\phi}{\partial\hat{t}}\delta_{ij} - \hat{\nu}\nabla^2\phi\delta_{ij}\right) = \frac{\partial g_i}{\partial\hat{t}} - \hat{\nu}\nabla^2 g_i. \tag{3.8}$$

Equation (3.8) simply expresses the condition necessary for (3.4) to correctly describe the large-scale dynamics embodied in the generalized velocity at finite pseudo-time. Because the residual stress should be disentangled from the (arbitrary) forcing function, both sides for (3.8) should be set to zero. Setting the right-hand side to zero, the generalized forcing function may be recognized as the Gaussian-filtered force, cf. (3.1*a*,*b*)

$$\frac{\partial g_i}{\partial\hat{t}} = \hat{\nu}\nabla^2 g_i, \quad g_i(\boldsymbol{x}, t; 0) = f_i(\boldsymbol{x}, t). \tag{3.9a,b}$$

The left-hand side of (3.8), once set to zero, may be simplified. Namely, the terms involving the generalized pressure, ϕ, may be removed on either of two considerations. First, the generalized pressure may be identified with the Gaussian-filtered pressure

$$\frac{\partial\phi}{\partial\hat{t}} = \hat{\nu}\nabla^2\phi, \quad \phi(\boldsymbol{x}, t; 0) = p(\boldsymbol{x}, t). \tag{3.10a,b}$$

Alternatively, and more generally, the dynamics of the generalized velocity depends only on the deviatoric part of the residual stress tensor, so any isotropic contribution can be safely ignored.

A sufficient condition for satisfying (3.8) and thus (2.11) is

$$\frac{\partial\sigma_{ij}}{\partial\hat{t}} = \hat{\nu}\nabla^2\sigma_{ij} + 2\hat{\nu}\frac{\partial w_i}{\partial x_k}\frac{\partial w_j}{\partial x_k}. \tag{3.11}$$

This is a forced diffusion equation in pseudo-time for $\boldsymbol{\sigma}$, and its formal solution in unbounded space is also readily obtained

$$\sigma_{ij}(\boldsymbol{x}, t; \hat{t}) = \int_0^{\hat{t}}\left[\iiint \frac{1}{(4\pi\hat{\nu}(\hat{t}-t'))^{3/2}}\exp\left(-\frac{|\boldsymbol{r}|^2}{4\hat{\nu}(\hat{t}-t')}\right)\frac{\partial w_i}{\partial x_k}\frac{\partial w_j}{\partial x_k}(\boldsymbol{x}+\boldsymbol{r}, t; t')\,\mathrm{d}\boldsymbol{r}\right]\mathrm{d}t'. \tag{3.12}$$

The residual stress at pseudo-time $\hat{t}$ may thus be interpreted as an integral over all earlier pseudo-times, $0 \le t' \le \hat{t}$, of the velocity gradient product at t' smoothed by a pseudo-viscosity from its earlier pseudo-time up until the pseudo-time at which the residual stress is evaluated, i.e. over the pseudo-time range $\hat{t} - t'$.

3.3. *Insights into the energy cascade*

The equivalence of PIC with Gaussian spatial filtering may be invoked, in the case of unbounded flows with uniform resolution, to rephrase the subfilter stress tensor of filtering

https://doi.org/10.1017/jfm.2021.1150 Published online by Cambridge University Press

theory in terms of multiscale velocity gradients. Dividing equation (3.11) by $2\hat{\nu}$, with the established relation $\ell^2 = 2\hat{\nu}\hat{t}$

$$\frac{\partial \tau_{ij}}{\partial(\ell^2)} = \frac{1}{2}\nabla^2\tau_{ij} + \frac{\partial \bar{u}_i^\ell}{\partial x_k}\frac{\partial \bar{u}_j^\ell}{\partial x_k}, \tag{3.13}$$

therefore has a formal solution, (3.12), that can itself be written in terms of an integral of Gaussian-filtered velocity gradients at all scales $0 \le \sqrt{\alpha} \le \ell$

$$\tau_{ij} = \int_0^{\ell^2} \overline{\frac{\partial \bar{u}_i^{\sqrt{\alpha}}}{\partial x_k}\frac{\partial \bar{u}_j^{\sqrt{\alpha}}}{\partial x_k}}^{\beta}\,\mathrm{d}\alpha, \tag{3.14}$$

where $\beta = \sqrt{\ell^2 - \alpha}$ is the width of the complementary filter which smooths from scale $\sqrt{\alpha}$ to scale ℓ.

Invoking the definition of the generalized second moment from Germano (1992)

$$\tau^\ell(a, b) = \overline{ab}^\ell - \bar{a}^\ell \bar{b}^\ell, \tag{3.15}$$

of which the subfilter stress tensor is one special case $\tau_{ij} = \tau(u_i, u_j)$, the PIC-based phrasing of the Gaussian filter's stress tensor can be split into resolved-scale and subfilter-scale contributions

$$\tau_{ij} = \ell^2 \frac{\partial \bar{u}_i^\ell}{\partial x_k}\frac{\partial \bar{u}_j^\ell}{\partial x_k} + \int_0^{\ell^2} \tau^\beta\left(\frac{\partial \bar{u}_i^{\sqrt{\alpha}}}{\partial x_k}, \frac{\partial \bar{u}_j^{\sqrt{\alpha}}}{\partial x_k}\right)\mathrm{d}\alpha. \tag{3.16}$$

The first of the two terms on the right-hand side is the nonlinear gradient model, which by itself performs well in *a priori* testing compared with eddy viscosity models (Clark *et al.* 1979; Borue & Orszag 1998). The second term shows how such a model leaves out smaller-scale (unresolved) content. Further decomposing the filtered velocity gradients in (3.16) into strain rate and vorticity, and forming the product $\Pi^\ell = -\tau_{ij}^\ell \bar{s}_{ij}^\ell$, the local energy cascade rate may be written in terms of vorticity stretching and strain self-amplification

$$\Pi^\ell = \Pi_{s1}^\ell + \Pi_{\omega 1}^\ell + \Pi_{s2}^\ell + \Pi_{\omega 2}^\ell + \Pi_c^\ell, \tag{3.17}$$

where

$$\Pi_{s1}^\ell = -\ell^2 \bar{s}_{ij}^\ell \bar{s}_{jk}^\ell \bar{s}_{ki}^\ell = \text{strain-rate self-amplification at scale } \ell, \tag{3.18}$$

$$\Pi_{\omega 1}^\ell = \frac{1}{4}\ell^2 \bar{s}_{ij}^\ell \bar{\omega}_i^\ell \bar{\omega}_j^\ell = \text{vorticity stretching at scale } \ell, \tag{3.19}$$

$$\Pi_{s2}^\ell = -\bar{s}_{ij}^\ell \int_0^{\ell^2} \tau_\beta(\bar{s}_{jk}^{\sqrt{\alpha}}, \bar{s}_{ki}^{\sqrt{\alpha}})\,\mathrm{d}\alpha = \text{multiscale strain amplification by strain at } \ell, \tag{3.20}$$

$$\Pi_{\omega 2}^\ell = \bar{s}_{ij}^\ell \int_0^{\ell^2} \tau_\beta(\bar{\omega}_i^{\sqrt{\alpha}}, \bar{\omega}_j^{\sqrt{\alpha}})\,\mathrm{d}\alpha = \text{multiscale vorticity stretching by strain at } \ell, \tag{3.21}$$

$$\Pi_c^\ell = 2\bar{s}_{ij}^\ell \int_0^{\ell^2} \tau_\beta(\bar{s}_{jk}^{\sqrt{\alpha}}, \bar{\Omega}_{ki}^{\sqrt{\alpha}})\,\mathrm{d}\alpha = \text{multiscale vortex thinning by strain at } \ell. \tag{3.22}$$

In this way, the rephrasing of spatial filtering in terms of PIC for unbounded flows with uniform resolution leads to a unique theoretical insight: the exact relation of commonly

https://doi.org/10.1017/jfm.2021.1150 Published online by Cambridge University Press

invoked mechanisms to the energy cascade. For more details, the reader is referred to Johnson (2020, 2021*a*). A treatment of the topic for a broader audience is given in Johnson (2021*b*).

DNS of homogeneous isotropic turbulence demonstrates that the multiscale gradient terms in $\boldsymbol{\tau}$ align closely with the filtered strain-rate tensor (Johnson 2021*a*). The eddy viscosity model is thus a good approximation for the second term on the right-hand side of (3.16). Overall, this suggests the applicability of a mixed model, with $\boldsymbol{\sigma} = \boldsymbol{\tau}$ being the sum of nonlinear gradient and eddy viscosity terms (Vreman *et al.* 1994).

3.4. *An alternative to the Germano identity*

The dynamic procedure (Germano *et al.* 1991) based on the Germano identity (Germano 1992) is one of the most common direct uses of spatial filtering theory in LES practice. The basic idea is that coefficients for a given model may be estimated from the resolved scales using a test filter larger than the grid size. A similar procedure may be developed with PIC via the dependence of $\boldsymbol{\sigma}$ on the cutoff scale (i.e. pseudo-time).

This may be briefly demonstrated for a generic eddy viscosity model

$$\sigma_{ij}^{(d)} \approx -2\nu_T S_{ij}. \tag{3.23}$$

First, (3.23) is substituted into (3.11) and the spatial variability of ν_T is neglected (for convenience, as commonly done for the Smagorinsky coefficient)

$$-2S_{ij}\frac{\partial \nu_T}{\partial \hat{t}} = 2\hat{\nu}\left(\frac{\partial w_i}{\partial x_k}\frac{\partial w_j}{\partial x_k} - \frac{1}{3}\frac{\partial w_m}{\partial x_n}\frac{\partial w_m}{\partial x_n}\delta_{ij}\right). \tag{3.24}$$

The above expression may be modified to the Smagorinsky form and the spatial variability of the filtered strain rate may also be factored in, if desired.

Second, Kolmogorov (1941) scaling is assumed, $\nu_T \sim \ell^{4/3} \sim \hat{t}^{2/3}$, so that the variation of the eddy viscosity in pseudo-time may be evaluated, $\partial \nu_T/\partial \hat{t} = \frac{2}{3}(\nu_T/\hat{t})$. Then (3.26) becomes

$$-\frac{4}{3}S_{ij}\nu_T = \ell^2\left(\frac{\partial w_i}{\partial x_k}\frac{\partial w_j}{\partial x_k} - \frac{1}{3}\frac{\partial w_m}{\partial x_n}\frac{\partial w_m}{\partial x_n}\delta_{ij}\right), \tag{3.25}$$

where $\ell^2 = 2\hat{\nu}\hat{t}$. This equation is over-determined because, in general, a scalar ν_T will not be found that can satisfy the full tensor equation. Therefore, as is typical for dynamic procedures, a least-squares procedure is employed (Lilly 1992). This step leads to a projection on S_{ij} that carries the physical meaning of matching the energy cascade rate. The resulting expression for the eddy viscosity is

$$\nu_T = \frac{3\ell^2}{4}\frac{A_{ik}A_{jk}A_{ij}}{S_{mn}S_{mn}} = \frac{3\ell^2}{4}\frac{\frac{1}{4}W_i S_{ij} W_j - S_{ij}S_{jk}S_{ki}}{S_{mn}S_{mn}}, \tag{3.26}$$

where $A_{ij} = \partial w_i/\partial x_j$ is the generalized velocity gradient tensor, $S_{ij} = \frac{1}{2}(A_{ij} + A_{ji})$ is the generalized strain-rate tensor and $W_i = \epsilon_{ijk}A_{kj}$ is the generalized vorticity. The denominator of this relation is positive–definite. The numerator represents the sum of vortex stretching and strain-rate self-amplification, which is positive on average for turbulent flows. Local negative values of the numerator may necessitate averaging or clipping strategies as done in the Germano-based dynamic procedure.

Johnson (2021*a*) demonstrated that the eddy viscosity approximation is more physically accurate for the only part of the residual stress tensor

$$e_{ij} = \sigma_{ij} - 2\hat{\nu}\hat{t}\frac{\partial w_i}{\partial x_k}\frac{\partial w_j}{\partial x_k}, \tag{3.27}$$

which represents multiscale vortex stretching and strain-rate amplification in (3.16). It may be shown from (3.1*a*,*b*) and (3.11) that

$$\frac{\partial e_{ij}}{\partial \hat{t}} = \hat{\nu}\nabla^2 e_{ij} + 4\hat{\nu}^2\hat{t}\frac{\partial^2 w_i}{\partial x_m \partial x_n}\frac{\partial^2 w_j}{\partial x_m \partial x_n}. \tag{3.28}$$

Substituting the eddy viscosity approximation, (3.23), for $e_{ij}^{(d)}$ rather than the full residual stress tensor, $\sigma_{ij}^{(d)}$, and again assuming $\nu_T \sim \hat{t}^{2/3}$ with a least-squares approach leads to a 'dynamic' mixed model

$$\sigma_{ij}^{(d)} = \ell^2 (A_{ik}A_{jk})^{(d)} - 2\nu_T S_{ij}, \quad \nu_T = -\frac{3\ell^4}{4}\frac{B_{ikl}S_{ij}B_{jkl}}{S_{mn}S_{mn}}, \tag{3.29a,b}$$

where $B_{ijk} = \partial^2 w_i/\partial x_j \partial x_k$ and $\ell^2 = 2\hat{\nu}\hat{t}$. The appearance of the second derivative of the generalized velocity field in the mixed model is less practical when numerical errors are inherent in assessing spatial derivatives. Nonetheless, (3.29*a*,*b*) provides a useful initial test for assessing the relative strengths of PIC theory.

3.5. *A priori testing*

DNS of homogeneous isotropic turbulence is used for *a priori* tests reported in this subsection. The incompressible Navier–Stokes equation, (2.1), is solved using a pseudo-spectral method with 1024 collocation points in each direction. The fully resolved velocity field, $\boldsymbol{u}$, is advanced in time with a second-order Adams–Bashforth scheme, and the pressure p simply enforces the divergence-free condition. The $2\sqrt{2}/3$ rule for wavenumber truncation is used with phase-shift dealiasing (Patterson & Orszag 1971). The forcing, $\boldsymbol{f}$, is specifically designed to maintain constant kinetic energy in the first two wavenumber shells.

The simulation was initialized using a Gaussian random velocity field satisfying a model turbulent energy spectrum (Pope 2000). The simulation was first run through a startup period to reach statistical stationarity. Then, statistics are computed over six large-eddy turnover times. The Taylor-scale Reynolds number is approximately $Re_\lambda = 400$ with grid resolution $k_{max}\eta = 1.4$. The integral length scale is approximately 20 % of the periodic box size of 2π and $L/\eta = 460$. The skewness of the longitudinal velocity gradient is -0.58, and the flatness of the longitudinal and transverse velocity gradients are 8.0 and 12.4, respectively, in reasonable agreement with previous simulations (Ishihara *et al.* 2007). The *a priori* assessment is carried out for the 'dynamic' viscosity model, (3.26), and 'dynamic' mixed model, (3.29*a*,*b*), along with existing popular models including the standard dynamic Smagorinsky model (Germano *et al.* 1991; Lilly 1992) and nonlinear gradient model (Clark *et al.* 1979; Borue & Orszag 1998). For all three dynamic models, spatial averaging is used for the numerator and denominator of the Smagorinsky coefficient or eddy viscosity. The results are shown in figure 2. For this case, PIC and Gaussian filtering are equivalent so the language of each approach is used interchangeably.

Perhaps the most important practical consideration for LES models is providing the proper rate of energy removal to unresolved scales. Figure 2(*a*) shows the average cascade

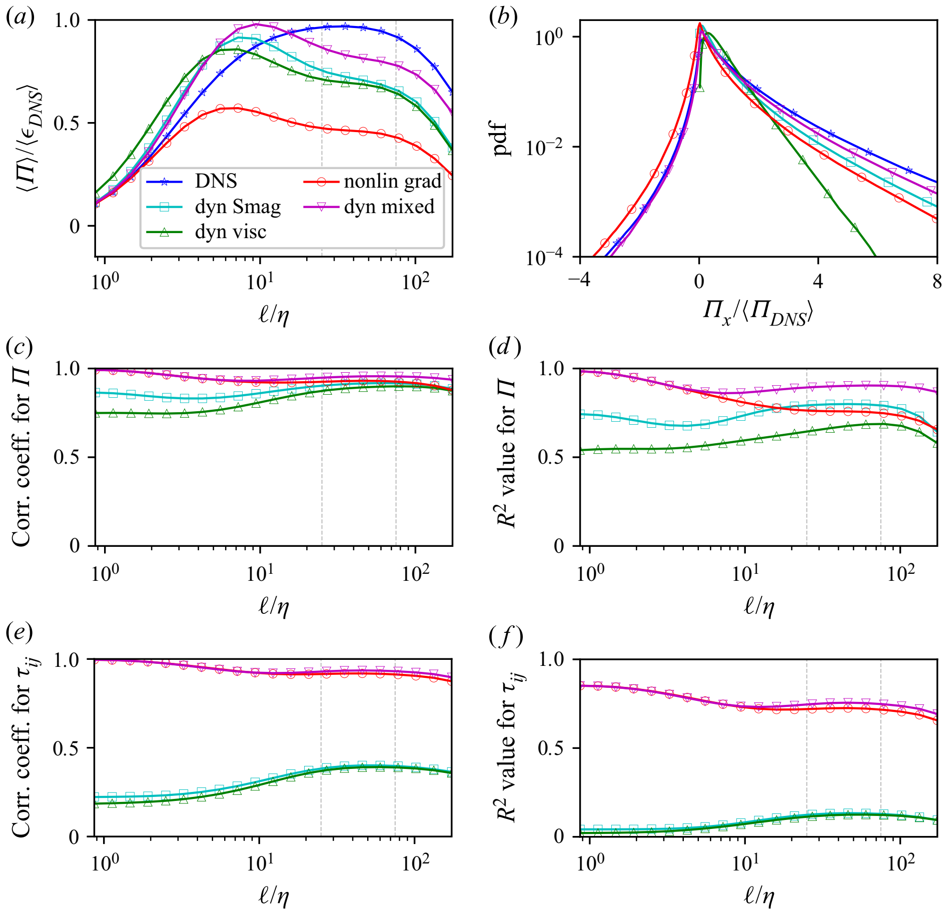

Figure 2. *A priori* comparison of new dynamic eddy viscosity ('dyn visc') and dynamic mixed ('dyn mixed') models with DNS results and existing models: dynamic Smagorinsky ('dyn Smag') and nonlinear gradient model ('nonlin grad'): (*a*) mean cascade rate, (*b*) probability density function of energy cascade rate at $\ell = 46\eta$, (*c*,*d*) correlation coefficient and R^2 coefficient (also known as the coefficient of determination) for the energy cascade rate, respectively, (*e*,*f*) correlation coefficient and R^2 coefficient for the full residual stress tensor, respectively. Two vertical dashed grey lines indicate rough bounds for the approximate inertial subrange of scales in the DNS, $25 \leq \ell/\eta \leq 75$.

rate, Π, as a function of filter width, $\ell = \sqrt{2\hat{\nu}\hat{t}}$, normalized by the average dissipation rate in the unfiltered DNS. The blue curve with star symbols shows that the cascade rate is nearly equal to the dissipation rate for $25 \lesssim \ell/\eta \lesssim 75$, an approximate inertial range for the simulation. The cascade rate decays to zero as ℓ decreases because viscous dissipation becomes significant near the Kolmogorov scale. The other four curves indicate the extent to which the four models reproduce the correct cascade rate when applied directly to coarsened DNS data. As is well known, the nonlinear gradient model is under-dissipative, especially in the inertial range, and the dynamic Smagorinsky model provides a better approximation of the energy removal rate. The PIC-based dynamic eddy viscosity model performs very similarly to the filter-based dynamic Smagorinsky model. The PIC-based dynamic mixed model is confirmed to remove energy at a higher rate in the inertial range than the nonlinear gradient or eddy viscosity models on their own.

https://doi.org/10.1017/jfm.2021.1150 Published online by Cambridge University Press

The probability density function (PDF) of the energy cascade rate, Π, for each model at $\ell = 46\eta$ is shown in figure 2(*b*) along with the coarsened DNS result. The DNS data indicate the existence of some backscatter, but the distribution is strongly skewed toward positive cascade rates. The two eddy viscosity models do not allow any backscatter by construction due to the spatial averaging used as part of the dynamic procedure. The nonlinear gradient and PIC-based dynamic mixed model provide relatively appropriate probabilities of backscatter, with the mixed model having the best overall agreement with DNS.

Figures 2(*c*) and 2(*d*) show the correlation coefficient and R-squared value based on each model's point-by-point prediction of the cascade rate, Π. An R-squared value of one indicates a perfect model. All four models are highly correlated with DNS in the inertial range, but the absolute error measured by the R-squared value shows more variation in the models performances. Both metrics show that the PIC-based dynamic mixed model is in closest agreement with DNS. Figures 2(*e*) and 2(*f*) show the correlation coefficients and R-squared values based on the full residual (subfilter) stress tensor. The stress tensor is known to align poorly with the strain-rate tensor, so the eddy viscosity models perform poorly for both metrics. The nonlinear gradient model performs quite well and the dynamic mixed model shows only slight improvement. The major benefit of the mixed model over the nonlinear gradient model has already been demonstrated in figure 2(*a*).

3.6. *A posteriori testing*

LESs were performed using three stress models: Smagorinsky, PIC-based dynamic eddy viscosity (3.26), and PIC-based dynamic mixed (3.29*a*,*b*). The same pseudo-spectral code from the DNS is used. The Smagorinsky coefficient is not determined dynamically for the LES, but was manually chosen to produce accurate results. For the two PIC-based dynamic models, spatial averaging is used for the numerator and denominator of the eddy viscosity, so that the eddy viscosity does not vary in space for either. As such, the simulation with the PIC-based dynamic eddy viscosity model is essentially a DNS at a lower Reynolds number, with the PIC-based theory setting the viscosity so as to match Gaussian-filtered DNS (fDNS) with a given filter width.

The filter width (pseudo-time) is chosen to be $\ell/\eta = 24$, which is at the small-scale end of the inertial range identified in the *a priori* tests. The following grid resolutions were tested: 64^3, 128^3 and 256^3. These correspond to $k_{max}\ell = 1.5$, 3.0 and 6.0. The DNS results are filtered with a Gaussian kernel (equivalent to PIC) for direct comparison with the LES results from each model. Figure 3(*a*) shows the energy spectra from LES simulations at each of the three resolutions with the PIC-based dynamic eddy viscosity model. The spectra from each resolution overlap until wavenumbers close to k_{max}, where a slight pileup occurs. The results from 128^3 and 256^3 are very similar, indicating grid convergence, but 64^3 is not grid converged. The spectra from the three models are compared at 128^3 resolution in figure 3(*b*). The Smagorinsky model is known to produce a spectrum close to that of a Gaussian filter (Pope 2000), as affirmed by the results here. The PIC-based dynamic mixed model produces a spectrum almost indistinguishable from the Gaussian-filtered DNS for the simulation shown here. All three models produce spectra in reasonable agreement. The PIC-based dynamic procedure for determining the eddy viscosity is thus shown to work well for both the pure eddy viscosity and mixed models.

In addition to testing the energy spectra produced by various LES models, it is also useful to compare local flow topology statistics. Given the importance of strain self-amplification and vorticity stretching to turbulence dynamics, the LES models are

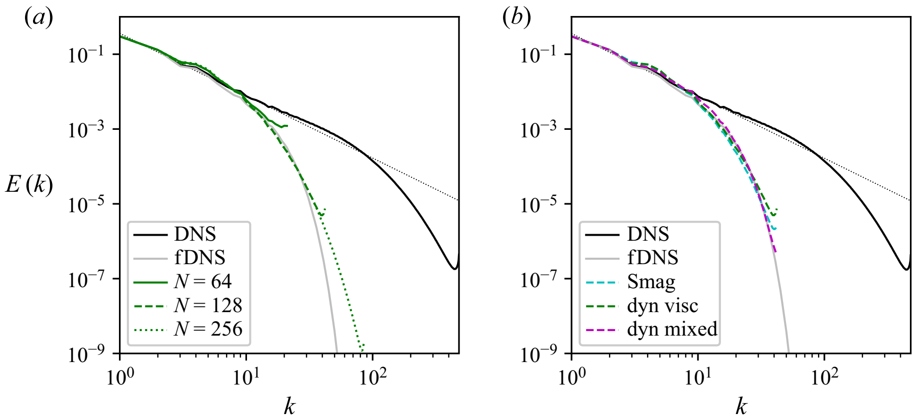

Figure 3. Energy spectra for *a posteriori* testing: (*a*) using PIC-based dynamic eddy viscosity model with $\ell/\eta = 24$ at three different resolutions, and (*b*) using three different models with $k_{max}\ell = 3$. A Kolmogorov spectrum, $E(k) = 1.6\epsilon^{2/3}k^{-5/3}$ is shown for reference in both panels.

compared with filtered DNS in terms of the following two quantities:

$$s^* = \frac{-\sqrt{6}S_{ij}S_{jk}S_{ki}}{(S_{mn}S_{mn})^{3/2}} \quad \omega^* = \frac{\sqrt{6}W_i S_{ij} W_j}{2W_k W_k (S_{mn}S_{mn})^{1/2}}. \tag{3.30a,b}$$

The first, s^*, was introduced by Lund & Rogers (1994) and quantifies the efficiency of the strain self-amplification contribution to the energy cascade, $-1 \leq s^* = \Pi_{s1}/\Pi_{s1,max} \leq 1$. The second term likewise indicates the efficiency of the vorticity stretching contribution to the cascade, $-1 \leq \omega^* = \Pi_{\omega 1}/\Pi_{\omega 1,max} \leq 1$. The concept of cascade efficiency was introduced by Ballouz & Ouellette (2018) and extended to include the above definitions in Johnson (2021*a*). These two quantities describe flow topology in a way most relevant to turbulent cascade physics.

Figure 4 compares the PDFs of s^* and ω^* from LES models and filtered DNS. Results from unfiltered DNS are also shown to highlight the similarity of the eddy viscosity models, particularly the PIC-based dynamic viscosity model, with (unfiltered) DNS. The reason for this is that the eddy viscosity models behave like DNS at lower Reynolds numbers, and thus produce topology statistics similar to the Kolmogorov scales in DNS. However, the results in figure 4 demonstrate that the PIC-based mixed model captures subtle physical differences between viscous-scale and inertial range flow topology statistics.

Many other metrics can be used to judge the *a posteriori* accuracy of LES models. It is not the goal at present to thoroughly explore all possibilities. However, a number of highly relevant statistics are summarized in table 1. It may be noted that the PIC-based dynamic mixed model slightly over-predicts the magnitude of velocity gradients, which may also be noticed in the spectra shown in figure 3(*b*), where a slight over-prediction is noticeable for a range of wavenumbers slightly smaller than the inverse of the filter scale. There appears to be a slight (unphysical) build up of energy not entirely unlike the bottleneck effect commonly observed in DNS and experimental data near the Kolmogorov scale (Falkovich 1994; Donzis & Sreenivasan 2010).

All three models over-predict the fraction of the cascade rate due to single-scale strain self-amplification and vorticity stretching. For the mixed model, this shows that too much energy removal is done through the nonlinear gradient term, and not enough through the

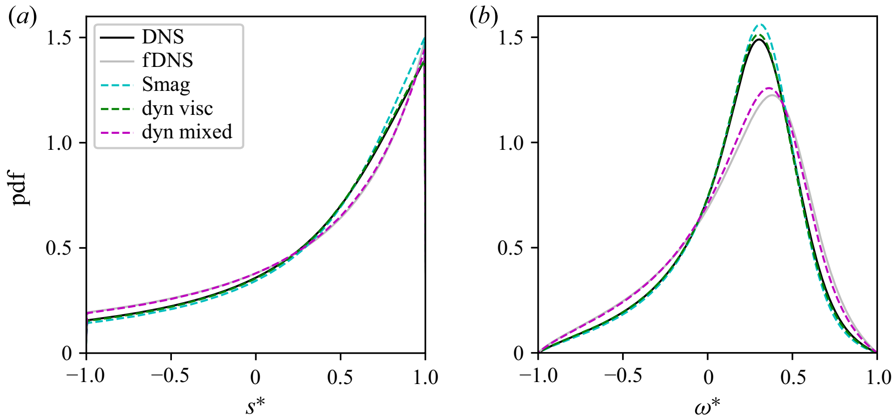

Figure 4. PDFs of s^* and ω^*, (3.30*a,b*), for LES with three different models compared with DNS and filtered DNS.

Model	$\langle S_{ij}S_{ij}\rangle\tau_\eta^2$	$\langle\Pi_{s1}\rangle/\langle\Pi\rangle$	$\langle\Pi_{\omega1}\rangle/\langle\Pi\rangle$	$\langle A_{11}^3\rangle/\langle A_{11}^2\rangle^{3/2}$	$\langle A_{11}^4\rangle/\langle A_{11}^2\rangle^2$	$\langle A_{12}^4\rangle/\langle A_{12}^2\rangle^2$
fDNS	1.7e − 2	0.37	0.12	−0.41	3.9	4.6
Smag.	1.8e − 2	0.42	0.14	−0.42	3.6	4.9
Dyn. visc.	1.9e − 2	0.50	0.17	−0.47	4.7	6.7
Dyn. mixed	1.9e − 2	0.45	0.15	−0.41	4.0	4.9

Table 1. Statistical results from LES and filtered DNS at $\ell/\eta = 24$ with 128^3 resolution ($k_{max}\ell = 3$). These values were converged when compared with 256^3 resolution.

eddy viscosity. The longitudinal and transverse velocity gradient skewness and flatness values from the mixed model LES are in fairly good agreement with the filtered DNS. Notice that the dynamic eddy viscosity model leads to too much intermittency (higher skewness and flatness), because it has a spatially uniform eddy viscosity, whereas the local adjustments due to Smagorinsky's eddy viscosity bring intermittency metrics more in line with filtered DNS.

Overall, all three models perform reasonably well in *a posteriori* tests. Furthermore, the relative advantages of the mixed model are clear, and the success of the PIC-based dynamic scheme is demonstrated. It should be appreciated that PIC theory for LES can facilitate model development well beyond the specific models tested here. The success of these models, however, does motivate future work to develop refined PIC-based models.

4. Toward PIC for more complex flows

In § 3, it was shown that PIC is mathematically equivalent to spatial filtering with a Gaussian kernel for unbounded flows with uniform, isotropic resolution. Even so, the PIC-based approach to LES provided theoretical and modelling insights, including a PIC-based alternative to the Germano-based dynamic procedure that does not require test filtering. Preliminary models showed promising *a priori* and *a posteriori* results, but there is more room for future work developing and testing models even for that simple case.

In this section, the extension of PIC to a number of more complex flow scenarios is outlined. The focus is on how the basic theory of PIC provides the flexibility and

https://doi.org/10.1017/jfm.2021.1150 Published online by Cambridge University Press

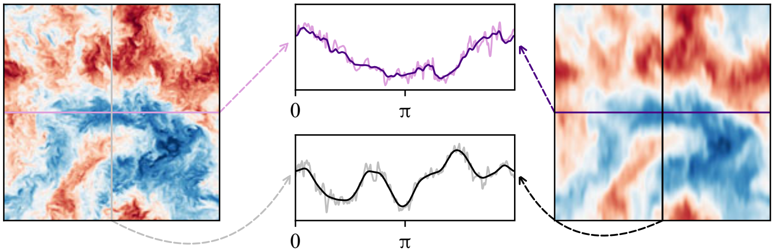

Figure 5. A coarsened velocity field using anisotropic pseudo-viscosity on DNS data of homogeneous isotropic turbulence. The resolution length scale ($\sqrt{2\hat{\nu}\hat{t}}$) in the x direction (purple/magenta lines) is one-fourth of that in the y direction (black/grey lines).

systematic approach to incorporate features needed for practical application of LES to complex flows.

4.1. *Anisotropic resolution*

The first step toward LES of more complex flows is a consistent treatment of grid anisotropy. Anisotropic grid resolutions are often unavoidable in simulations with complex geometries. Various treatments of grid anisotropy exist for spatial filtering theory (Bardina *et al.* 1980; Scotti, Meneveau & Lilly 1993; Vreman 2004; Rozema *et al.* 2015; Haering, Lee & Moser 2019). In practice, simple treatments of grid anisotropy are common, such as using a scalar measure for effective resolution based on a suitable average of resolution in three different directions on an orthogonal grid: Δ_1, Δ_2 and Δ_3. Deardorff (1970) suggested the use of $\Delta = \sqrt[3]{\Delta_1\Delta_2\Delta_3}$ based on the cell volume and Bardina *et al.* (1980) used $\Delta = \sqrt{(\Delta_1^2 + \Delta_2^2 + \Delta_3^2)/3}$.

For viscosity-based smoothing, anisotropic resolution is easily introduced using a tensorial pseudo-viscosity aligned with the principal directions of the grid. Thus, (3.1*a*) for unbounded flows may be modified to incorporate anisotropic resolution effects

$$\frac{\partial w_i}{\partial \hat{t}} = \hat{\nu}_{jk}\frac{\partial^2 w_i}{\partial x_j \partial x_k}, \quad \frac{\partial w_j}{\partial x_j} = 0. \tag{4.1a,b}$$

For uniform resolution, the pseudo-pressure will satisfy the Laplace equation and hence be $\hat{p} = 0$ in the absence of flow boundaries. In that case, the result will be anisotropic Gaussian filtering aligned with the grid

$$w_i(\boldsymbol{x}, t; \hat{t}) = \iiint \frac{1}{\sqrt{(2\pi)^3 \det \boldsymbol{C}}} \exp\left(-\frac{1}{2} r_j C_{jk}^{-1} r_k\right) u_i(\boldsymbol{x} + \boldsymbol{r}, t)\, \mathrm{d}\boldsymbol{r}. \tag{4.2}$$

Here, the covariance tensor, $C_{ij} = 2\hat{\nu}_{ij}\hat{t}$, is equivalent to the moment of inertial tensor of Bardina *et al.* (1980). The isotropic form, (3.1*a,b*), is recovered when $\hat{\nu}_{ij} = \hat{\nu}\delta_{ij}$. The eigenvalues of $\boldsymbol{C}$, $\ell_{1,2,3}^2 = 2\hat{\nu}_{1,2,3}\ \hat{t}$, represent the (square of the) resolution in three directions given by their respective eigenvectors (e.g. the local coordinate frame of an orthogonal grid). The result of anisotropic PIC (i.e. anisotropic Gaussian filtering) is illustrated in figure 5. In this case, the coarsening procedure generates anisotropy in the generalized velocity field from an initially isotropic fully resolved velocity field (Haering *et al.* 2019).

https://doi.org/10.1017/jfm.2021.1150 Published online by Cambridge University Press

Substituting equations (2.8) and (4.1*a*,*b*) in (2.11), one obtains

$$\frac{\partial \sigma_{ij}}{\partial \hat{t}} = \hat{\nu}_{mn}\frac{\partial^2 \sigma_{ij}}{\partial x_m \partial x_n} + \hat{\nu}_{mn}\left(\frac{\partial w_i}{\partial x_m}\frac{\partial w_j}{\partial x_n} + \frac{\partial w_i}{\partial x_n}\frac{\partial w_j}{\partial x_m}\right). \tag{4.3}$$

The details of the derivation leading to (4.3) follow the same steps as those shown in § 3 leading to (3.11). Indeed, it is readily verified that (3.11) is recovered in the isotropic limit, $\hat{\nu}_{ij} = \hat{\nu}\delta_{ij}$. The PIC-based dynamic procedure for anisotropic grids can be based on (4.3), which could lead to eddy viscosity models that share some similarities with the anisotropic minimum dissipation model (Rozema *et al.* 2015) and the M43 model (Haering *et al.* 2019), while a PIC-based dynamic mixed model may share similarities with that of Vreman (2004).

4.2. *Non-uniform resolution*

Uniform grid resolution is useful for some simple canonical turbulent flows, but it is not practical for many naturally occurring and engineered flows. As discussed in the introduction, a non-uniform filter does not commute with spatial differentiation, giving rise to additional terms in the governing equations for filtered fields (Ghosal & Moin 1995; Yalla *et al.* 2021). Most notably, the filtered velocity field is no longer divergence free (Langford & Moser 2001).

In contrast, the PIC approach to the LES equations explicitly enforces a divergence-free condition on the generalized velocity field, $\boldsymbol{w}$, using a pseudo-pressure, $\hat{p}$, in the auxiliary evolution equation in pseudo-time, $\hat{t}$. The above theory for uniform resolution was able to ignore the proposed pseudo-pressure due to the form of its Poisson equation, (2.5), which may be alternatively written in terms of pseudo-viscosity gradients

$$\nabla^2 \hat{p} = 2\frac{\partial \hat{\nu}}{\partial x_i}\nabla^2 w_i + \frac{\partial^2 \hat{\nu}}{\partial x_i \partial x_j}\left(\frac{\partial w_i}{\partial x_j} + \frac{\partial w_j}{\partial x_i}\right), \tag{4.4}$$

which reduces to a Laplace equation for uniform pseudo-viscosity (i.e. uniform grid resolution). Non-uniform resolution is represented as spatial variation of the pseudo-viscosity, $\hat{\nu} = \hat{\nu}(\boldsymbol{x})$, which activates a non-zero pseudo-pressure to enforce the divergence-free condition. Note that, with the non-zero pseudo-pressure, the PIC equations for pseudo-time evolution are no longer purely parabolic, but include an elliptic nature as well. However, the square-of-exponential falloff of the spectral content is still roughly preserved, so that the removal of small scales is still rather efficient compared with other elliptic partial differential equations (Germano 1986*a*,*b*; Bull & Jameson 2016).

Figure 6 demonstrates the outcome of PIC with a spatially varying pseudo-viscosity for a velocity field snapshot from DNS of homogeneous isotropic turbulence with $\hat{\nu}(y) = \hat{\nu}_{max} - (\hat{\nu}_{max} - \hat{\nu}_{min})\cos(y)$, where $0 \leq y \leq 2\pi$ is the vertical axis as printed on the page. The rightmost image is of a divergence-free velocity field with variable resolution. The effective resolution is isotropic, but varies in space, with high resolution near the top and bottom ($\hat{\nu} \approx \hat{\nu}_{min}$) and low resolution near the centre ($\hat{\nu} \approx \hat{\nu}_{max}$).

The case of non-uniform (isotropic) resolution is useful for reflecting on the PIC approach in general. The goal of PIC is to create LES equations with well-defined closure terms that facilitate effective modelling in ways that improve upon spatial filtering. It is not a central goal of PIC to remain particularly faithful to physical processes during its pseudo-time evolution. The physical processes inspiring the pseudo-time dynamics are useful insomuch as they create helpful representations for LES. This allows some freedom

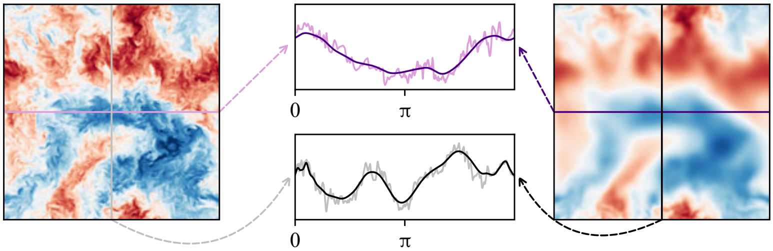

Figure 6. A (divergence-free) coarsened velocity field using sinusoidally varying pseudo-viscosity applied to DNS data of homogeneous isotropic turbulence. The resolution length scale, $\sqrt{2\hat{\nu}\hat{t}}$ varies by a factor of 4 between $y = 0$ and $y = \pi$.

when designing the details of PIC, for example, one may choose to simplify the auxiliary Stokes equation, (2.4), to

$$\frac{\partial w_i}{\partial \hat{t}} = -\frac{\partial \hat{p}}{\partial x_i} + \frac{\partial}{\partial x_j}\left[\hat{\nu}\frac{\partial w_i}{\partial x_j}\right], \quad \frac{\partial w_j}{\partial x_j} = 0, \quad \nabla^2 \hat{p} = \frac{\partial}{\partial x_j}\left(\frac{\partial \hat{\nu}}{\partial x_i}\frac{\partial w_i}{\partial x_j}\right). \tag{4.5a,b}$$

The difference between (2.4) and (4.5*a*,*b*) is only material for non-uniform pseudo-viscosity. Either may be used for PIC, and it is not immediately evident which will be most beneficial for LES. More research is needed to elucidate the relative strengths of either.

Substituting equations (4.5*a*,*b*) and (2.8) into (2.11) and performing simplifications like those in § 3, one may arrive at the auxiliary equation for the residual stress for general $\hat{\nu} = \hat{\nu}(\boldsymbol{x})$

$$\begin{aligned}\frac{\partial \sigma_{ij}}{\partial \hat{t}} &= \frac{\partial}{\partial x_k}\left(\hat{\nu}\frac{\partial \sigma_{ij}}{\partial x_k}\right) + 2\hat{\nu}\frac{\partial w_i}{\partial x_k}\frac{\partial w_j}{\partial x_k} \\ &\quad - \left(w_i\frac{\partial w_k}{\partial x_j} + w_j\frac{\partial w_k}{\partial x_i} + \frac{\partial w_i w_k}{\partial x_j} + \frac{\partial \sigma_{ik}}{\partial x_j} - \frac{\partial \hat{p}}{\partial x_j}\delta_{ik}\right)\frac{\partial \hat{\nu}}{\partial x_k} + (w_i\delta_{jk} + w_j\delta_{ik})\frac{\partial \hat{p}}{\partial x_k}.\end{aligned} \tag{4.6}$$

Deviations from (3.11) are proportional to the pseudo-viscosity gradient, as well as the pseudo-pressure. One way to view the extra terms in (4.6) is to view them as consequences of the lack a commutativity between multiplication by $\hat{\nu}$ and differentiation. The advantage of this PIC formulation is that these commutator terms are built into the residual stress, and so provide a path for extending the use of dynamic procedures and other approaches from uniform resolution to more general cases. Beyond traditional (theory-based) modelling approaches, data-driven techniques may stand to benefit even more from PIC and (4.6). While isotropic non-uniform resolution has been considered here, the same procedure may be used to combine anisotropic and non-uniform grid effects into a single formulation.

4.3. *Heat and mass transfer*

In addition to complexities introduced by numerical grid effects, PIC provides a holistic approach for reducing the computational DoFs needed to represent turbulence in regimes with additional physical effects beyond unbounded single-phase incompressible flows. The next few subsections touch briefly on a few examples, the simplest of which is passive scalar transport.

For flows with heat or mass transfer described by an advection diffusion equation

$$\frac{\partial T}{\partial t} + u_j \frac{\partial T}{\partial x_j} = \alpha \nabla^2 T, \tag{4.7}$$

the relevant scalar field T (e.g. temperature or concentration) may be coarsened in a physics-inspired manner using an pseudo-conductivity or pseudo-diffusivity, $\hat{\alpha}$, to form a generalized temperature/concentration, θ, with pseudo-time evolution given by an auxiliary heat equation

$$\frac{\partial \theta}{\partial \hat{t}} = \hat{\alpha} \nabla^2 \theta, \quad \frac{\partial \theta}{\partial t} + w_j \frac{\partial \theta}{\partial x_j} = \alpha \nabla^2 \theta - \frac{\partial q_j}{\partial x_j}, \tag{4.8a,b}$$

so that the physical time evolution of the generalized temperature/concentration must include a residual heat/mass flux $\boldsymbol{q}$. The equality of mixed partial derivatives for θ

$$\frac{\partial}{\partial \hat{t}} \left(\frac{\partial \theta}{\partial t} \right) = \frac{\partial}{\partial t} \left(\frac{\partial \theta}{\partial \hat{t}} \right), \tag{4.9}$$

may be satisfied by a forced diffusion equation for the residual heat/mass flux

$$\frac{\partial q_i}{\partial \hat{t}} = \hat{\alpha} \nabla^2 q_i + 2\hat{\alpha} \frac{\partial w_i}{\partial x_j} \frac{\partial \theta}{\partial x_j}. \tag{4.10}$$

Here, $\hat{\alpha} = \hat{\nu}$ is chosen (unity pseudo-Prandtl number) for convenience. Other choices of pseudo-Prandtl number are possible, but unlikely to be advantageous.

Similar extensions to non-uniform or anisotropic resolution may be found for heat/mass transfer as shown for the momentum equation above. Equation (4.10) can also provide insight into the scale-wise scalar fluctuation dynamics. A turbulent cascade of scalar variance may be linked to the multiscale squeezing of scalar filaments using the formal solution in wall-free flows following the procedure outline for the kinetic energy cascade in § 3. Furthermore, (4.10) can serve as the basis for a PIC-based dynamic procedure for an eddy diffusivity or mixed model for $\boldsymbol{q}$.

4.4. *Wall-bounded turbulent flows*

Turbulence near solid boundaries is very common in flows of interest for LES. This is the source of some inconvenience for spatial filtering theory. A uniform filter integral will require flow information outside the fluid domain (Drivas & Nguyen 2018; Kumar *et al.* 2021). This may be avoided through the use of a filter width which vanishes at the boundary is approached (Bose & Moin 2014), giving rise to commutation errors discussed in § 4.2.

In contrast to spatial filtering, the physics-inspired approach naturally extends to wall-bounded flows. To accomplish this, the auxiliary Stokes equation, (2.4) must be given boundary conditions for $\boldsymbol{w}$. For example, the use of user-defined boundary conditions for coarsening procedures has been preliminarily investigated (Bae & Lozano-Duran 2017, 2018). A number of choices are possible depending on the level of near-wall resolution. If the wall-normal grid spacing resolves the viscous sublayer, $\ell_y^+ \sim 1$, then the best choice of boundary conditions is likely Dirichlet, $\boldsymbol{w}|_{wall} = 0$. Depending on the wall parallel resolution, this approach could facilitate wall-resolved LES ($\ell_x^+ \sim \ell_z^+ \sim 50$) or near-wall RANS for hybrid RANS–LES (coarser x–z resolution).

Alternatively, a coarser wall-normal resolution, $\ell_y \gg 1$, would facilitate development of approximate closures for wall-modelled LES. In this case, Dirichlet boundary conditions could still be used (Bae & Lozano-Duran 2021), but other choices such as Robin (Bose & Moin 2014) or Neumann boundary conditions could be used. The choice of boundary conditions for the pseudo-time dynamics would directly set the boundary conditions to be used in LES on the generalized velocity field. Furthermore, complementary boundary conditions on the residual stress tensor, $\boldsymbol{\sigma}$, would also need to be specified in such a way as to preserve the integral of momentum transport across the boundary during the pseudo-time evolution so as to facilitate accurate calculations of forces in the LES. For example, in a wall-resolved LES regime, Dirichlet boundary conditions would likely be the best choice for the residual stress in conjunction with Dirichlet velocity boundary conditions. Further research is needed to determine the best approach for wall-modelled LES.

Data-driven techniques may be useful for testing the potential fruitfulness of various choices for the boundary conditions. For example, the art of constructing data-driven wall models may benefit substantially from the PIC-based approach to the LES equations. Sufficiently far from the wall, $y \gg \ell$, the PIC naturally recovers Gaussian filtering, but near the wall, the PIC theory outlined in this paper provides a method for determining how the choice of boundary conditions influences the residual stress tensor.

4.5. *Particle-laden flows*

Turbulent flows with small particles also represent a challenge to spatial filtering theory. Lagrangian particle tracking methods, in combination with an Eulerian representation of the carrier fluid, are increasingly common to computing particle-laden flows. In the PIC approach, the flow disturbance in the vicinity of the particle would be smoothed out, while boundary conditions may be freely chosen on the surface of the particle, as in the case of wall-bounded flows above. For example, choosing Neumann boundary conditions would, for particles smaller than the resolution length scale, $\ell \sim \sqrt{2\hat{\nu}\hat{t}}$, cause the carrier flow velocity on the surface of the particle to relax to that of the far-field coarsened velocity. This would be similar to the idea of recovering the 'undisturbed' fluid velocity upon which drag law formulations are based (Horwitz & Mani 2016, 2018; Balachandar, Liu & Lakhote 2019) generalized to the case in which the Kolmogorov scale is not captured by the grid. The considerations for particle-resolved calculations would be the same as for wall-bounded turbulence the previous subsection.

4.6. *Multiphase flows with resolved interfaces*

Multiphase turbulent flows include the additional complexity of moving discontinuities at phase interfaces with the accompanying surface tension force. Indeed, the interface is 'a critical feature of such flows and it is likely that coarsening of the flow must retain the interface, although probably with a simplified structure' (Tryggvason & Lu 2020). Difficulties arise in spatial filtering across discontinuities (Sagaut & Germano 2005; Toutant *et al.* 2009), and spatially filtering across fluid–fluid interfaces is not consistent with the typical (and desirable) sharp treatment of solid boundaries (walls) in LES. Indeed, spatial filtering across interfaces unnecessarily blurs essential physics at the interface, given the sophisticated numerical tools that have developed for treating sharp interfaces.

Various alternatives to spatial filtering for LES of multiphase flows have been proposed (see Lakehal (2018) and Chen, Lu & Tryggvason (2021) for a more thorough, up-to-date reviews). Herrmann (2013) proposed a dual-scale resolution procedure that requires

Figure 7. Sketch of how a pseudo-surface tension could create low DoF representations of a complex two-phase interface.

fine resolution of the interface embedded within coarser flow resolution. McCaslin & Desjardins (2014) suggested, but did not pursue, the idea of a surface filtering operation. Most recently, Chen *et al.* (2021) has advocated for a procedure very similar to the physics-inspired approach outlined here. Indeed, their approach, which specifically targets the use of data-driven modelling, could be thought of as one possibility within the PIC framework.

One possibility suggested by the physics-inspired philosophy is the use of an artificial surface tension along with the auxiliary Stokes equation to remove small-scale features. Physically speaking, surface tension limits the impact of turbulent motions on multiphase features (drops, bubbles, etc) smaller than the Hinze scale (Hinze 1955). Thus, just as the pseudo-viscosity artificially enhances the Kolmogorov scale, a pseudo surface tension acting during the pseudo-time evolution would likewise smooth small-scale interface curvature while transforming more abrupt small-scale features into spherical particles for Lagrangian particle tracking, see figure 7. Note that this PIC process would maintain a sharp interface treatment for features that can be captured on the coarse LES grid while creating low DoF representations for unresolved features. Such an approach provides a general framework to justify other existing heuristic approaches, e.g. for physics-based conversion of subgrid ligaments to point-particle representations (Kim & Moin 2020). The use of an artificial diffusion equation for Gaussian filtering has some precedence for simulating particle-laden flows (Capecelatro & Desjardins 2013). An artificial surface tension may also be a useful approach for treating multiscale (partially resolved) wall roughness.

5. Conclusions

In turbulence, viscosity provides a natural mechanism preventing motions smaller than the Kolmogorov scale. In this paper, it is proposed to view an LES velocity field as the result of (artificial) viscous smoothing rather than a spatial filtering operating. This approach is called PIC. In PIC, a pseudo-viscosity (and pseudo-pressure) acts in pseudo-time on an initially fully resolved snapshot of turbulence according to an auxiliary Stokes equation. The generalized velocity field is a function of both physical time and pseudo-time. The effective equations for the generalized velocity field in physical time (at a fixed pseudo-time corresponding to numerical resolution $\ell \sim \sqrt{2\hat{\nu}\hat{t}}$) provide the governing equations for LES. The equality of mixed partial derivatives in physical time and pseudo-time provides a consistency condition that defines the residual stress tensor based on the chosen pseudo-time evolution equation.

In the simple case of unbounded flow with uniform numerical resolution, PIC is shown to be equivalent to Gaussian filtering. Thus, the advantages of spatial filtering are retained while providing a basis for defining a more generally applicable coarsening procedure

https://doi.org/10.1017/jfm.2021.1150 Published online by Cambridge University Press

for complex flows. Even in the simple case of unbounded flows with uniform resolution, the PIC approach yields fresh insight. First, PIC leads to a previously hidden exact representation of the energy cascade in terms of multiscale velocity gradient interactions. This provides a more precise framework for representing residual stresses based on vortex stretching and other similar processes. Furthermore, the resulting parabolic PDE in pseudo-time may be used to construct a Germano-like dynamic procedure that does not require a test filter. This is demonstrated in the creation of a dynamic eddy viscosity and dynamic mixed model based on PIC equations. The performance of both models in *a priori* and *a posteriori* testing is demonstrated in homogeneous isotropic turbulence. The dynamic eddy viscosity model performs similarly to the commonly used Smagorinsky model and the relative advantages of the dynamic mixed model are illustrated.

For realistic flows where non-uniform grid resolution is desirable, the PIC framework for LES provides a nature-inspired mechanism for maintaining a divergence-free condition for incompressible flows while avoiding commutation errors (extra terms in the LES equations). In the case of wall-bounded flows, boundary conditions may be chosen, PIC provides a convenient definition of what it means to coarsen a flow in the vicinity of a domain boundary, and can theoretically facilitate various modes of near-wall resolution or modelling treatment. PIC theory is also easily extended for a consistent treatment of resolution anisotropy by using an anisotropic pseudo-viscosity.

Finally, it is suggested that the physics-inspired framework provides a promising direction for addressing with more complex physics. A simple example of such an extension is heat/mass transfer, for which the PIC approach to momentum can be straightforwardly copied. More significant extensions are also possible with PIC, such as particle-laden or (interface-resolved) multiphase flows. These possible extensions, for which the preliminary theory is discussed briefly here, require further research for detailed modelling and testing. While PIC provides theoretical developments that can aid model development for complex LES, it also provides an important foundation for enabling robust data-driven modelling approaches. Indeed, data-driven closure techniques may benefit significantly from the advantages of the PIC approach to LES theory, for example, the recovery of divergence-free coarsened velocity field for incompressible flows.

Declaration of interests. The author reports no conflict of interest.

Author ORCIDs.
Perry L. Johnson https://orcid.org/0000-0002-7929-9396.

References

Bae, H.J. & Lozano-Duran, A. 2017 Towards exact subgrid-scale models for explicitly filtered large-eddy simulation of wall-bounded flows. *Ann. Res. Br.* **2017**, 207–214.

Bae, H.J. & Lozano-Duran, A. 2018 DNS-aided explicitly filtered les of channel flow. *Ann. Res. Br.* **2018**, 197–207.

Bae, H.J. & Lozano-Duran, A. 2021 Effect of wall boundary conditions on a wall-modeled large-eddy simulation in a finite-difference framework. *Fluids* **6** (3), 112.

Balachandar, S. & Eaton, J.K. 2010 Turbulent dispersed multiphase flow. *Annu. Rev. Fluid Mech.* **42** (1), 111–133.

Balachandar, S., Liu, K. & Lakhote, M. 2019 Self-induced velocity correction for improved drag estimation in Euler–Lagrange point-particle simulations. *J. Comput. Phys.* **376**, 160–185.

Ballouz, J.G. & Ouellette, N.T. 2018 Tensor geometry in the turbulent cascade. *J. Fluid Mech.* **835**, 1048–1064.

Bardina, J., Ferziger, J. & Reynolds, W. 1980 Improved subgrid-scale models for large-eddy simulation. In *AIAA 13th Fluid & Plasma Dynamics Conference AIAA Paper* 80-1357.

BASSENNE, M., ESMAILY, M., LIVESCU, D., MOIN, P. & URZAY, J. 2019 A dynamic spectrally enriched subgrid-scale model for preferential concentration in particle-laden turbulence. *Intl J. Multiphase Flow* **116**, 270–280.

BECK, A., FLAD, D. & MUNZ, C.-D. 2019 Deep neural networks for data-driven LES closure models. *J. Comput. Phys.* **398**, 108910.

BODE, M., GAUDING, M., LIAN, Z., DENKER, D., DAVIDOVIC, M., KLEINHEINZ, K., JITSEV, J. & PITSCH, H. 2021 Using physics-informed enhanced super-resolution generative adversarial networks for subfilter modeling in turbulent reactive flows. *Proc. Combust. Inst.* **38** (2), 2617–2625.

BORUE, V. & ORSZAG, S.A. 1998 Local energy flux and subgrid-scale statistics in three-dimensional turbulence. *J. Fluid Mech.* **366**, 1–31.

BOSE, S.T. & MOIN, P. 2014 A dynamic slip boundary condition for wall-modeled large-eddy simulation. *Phys. Fluids* **26** (1), 015104.

BOSE, S.T. & PARK, G.I. 2018 Wall-modeled large-eddy simulation for complex turbulent flows. *Annu. Rev. Fluid Mech.* **50** (1), 535–561.

BOU-ZEID, E., MENEVEAU, C. & PARLANGE, M. 2005 A scale-dependent Lagrangian dynamic model for large eddy simulation of complex turbulent flows. *Phys. Fluids* **17** (2), 025105.

BULL, J.R. & JAMESON, A. 2016 Explicit filtering and exact reconstruction of the sub-filter stresses in large eddy simulation. *J. Comput. Phys.* **306**, 117–136.

CAPECELATRO, J. & DESJARDINS, O. 2013 An Euler–Lagrange strategy for simulating particle-laden flows. *J. Comput. Phys.* **238**, 1–31.

CHEN, X., LU, J. & TRYGGVASON, G. 2021 Interface retaining coarsening of multiphase flows. *Phys. Fluids* **33** (7), 073316.

CHENG, Y., GIOMETTO, M., KAUFFMANN, P., LIN, L., CAO, C., ZUPNICK, C., LI, H., LI, Q., ABERNATHEY, R. & GENTINE, P. 2019 Deep learning for subgrid-scale turbulence modeling in large-eddy simulations of the atmospheric boundary layer. arXiv:1910.12125.

CLARK, R.A., FERZIGER, J.H. & REYNOLDS, W.C. 1979 Evaluation of subgrid-scale models using an accurately simulated turbulent flow. *J. Fluid Mech.* **91** (1), 1–16.

DEARDORFF, J.W. 1970 A numerical study of three-dimensional turbulent channel flow at large Reynolds numbers. *J. Fluid Mech.* **41** (2), 453–480.

DOMARADZKI, J.A. & LOH, K.-C. 1999 The subgrid-scale estimation model in the physical space representation. *Phys. Fluids* **11** (8), 2330–2342.

DONZIS, D.A. & SREENIVASAN, K.R. 2010 The bottleneck effect and the Kolmogorov constant in isotropic turbulence. *J. Fluid Mech.* **657**, 171–188.

DRIVAS, T.D. & NGUYEN, H.Q. 2018 Onsager's conjecture and anomalous dissipation on domains with boundary. *SIAM J. Math. Anal.* **50** (5), 4785–4811.

DURAISAMY, K. 2021 Perspectives on machine learning-augmented Reynolds-averaged and large eddy simulation models of turbulence. *Phys. Rev. Fluids* **6**, 050504.

FALKOVICH, G. 1994 Bottleneck phenomenon in developed turbulence. *Phys. Fluids* **6** (4), 1411–1414.

FOX, R.O. 2003 *Computational Models for Turbulent Reacting Flows*. Cambridge University Press.

FREUND, A. & FERRANTE, A. 2021 Large-eddy simulation of droplet-laden decaying isotropic turbulence using artificial neural networks. *Intl J. Multiphase Flow* **142**, 103704.

FROHLICH, J. & VON TERZI, D. 2008 Hybrid LES/RANS methods for the simulation of turbulent flows. *Prog. Aerospace Sci.* **44** (5), 349–377.

GAMAHARA, M. & HATTORI, Y. 2017 Searching for turbulence models by artificial neural network. *Phys. Rev. Fluids* **2**, 054604.

GERMANO, M. 1986*a* Differential filters for the large eddy numerical simulation of turbulent flows. *Phys. Fluids* **29** (6), 1755–1757.

GERMANO, M. 1986*b* Differential filters of elliptic type. *Phys. Fluids* **29** (6), 1757–1758.

GERMANO, M. 1992 Turbulence: the filtering approach. *J. Fluid Mech.* **238**, 325–336.

GERMANO, M., PIOMELLI, U., MOIN, P. & CABOT, W.H. 1991 A dynamic subgrid-scale eddy viscosity model. *Phys. Fluids* A: *Fluid Dyn.* **3** (7), 1760–1765.

GHATE, A.S. & LELE, S.K. 2017 Subfilter-scale enrichment of planetary boundary layer large eddy simulation using discrete Fourier–Gabor modes. *J. Fluid Mech.* **819**, 494–539.

GHATE, A.S. & LELE, S.K. 2020 Gabor mode enrichment in large eddy simulations of turbulent flow. *J. Fluid Mech.* **903**, A13.

GHOSAL, S. & MOIN, P. 1995 The basic equations for the large eddy simulation of turbulent flows in complex geometry. *J. Comput. Phys.* **118** (1), 24–37.

HAERING, S.W., LEE, M. & MOSER, R.D. 2019 Resolution-induced anisotropy in large-eddy simulations. *Phys. Rev. Fluids* **4**, 114605.

HERRMANN, M. 2013 A sub-grid surface dynamics model for sub-filter surface tension induced interface dynamics. *Comput. Fluids* **87**, 92–101.

HERRMANN, M., KEDELTY, D. & ZIEGENHEIN, T. 2018 A dual-scale subgrid closure for les of phase interfaces in turbulent flows. In *Proceedings of the Summer Program, Center for Turbulence Research, Stanford University*, pp. 45–54.

HINZE, J.O. 1955 Fundamentals of the hydrodynamic mechanism of splitting in dispersion processes. *AIChE J.* **1** (3), 289–295.

HORWITZ, J.A.K. & MANI, A. 2016 Accurate calculation of stokes drag for point–particle tracking in two-way coupled flows. *J. Comput. Phys.* **318**, 85–109.

HORWITZ, J.A.K. & MANI, A. 2018 Correction scheme for point-particle models applied to a nonlinear drag law in simulations of particle–fluid interaction. *Intl J. Multiphase Flow* **101**, 74–84.

ISHIHARA, T., KANEDA, Y., YOKOKAWA, M., ITAKURA, K. & UNO, A. 2007 Small-scale statistics in high-resolution direct numerical simulation of turbulence: Reynolds number dependence of one-point velocity gradient statistics. *J. Fluid Mech.* **592**, 335–366.

JOHNSON, P.L. 2020 Energy transfer from large to small scales in turbulence by multi-scale nonlinear strain and vorticity interactions. *Phys. Rev. Lett.* **124**, 104501.

JOHNSON, P.L. 2021*a* On the role of vorticity stretching and strain self-amplification in the turbulence energy cascade. *J. Fluid Mech.* **922**, A3.

JOHNSON, P.L. 2021*b* The squeezes, stretches, and whirls of turbulence. *Phys. Today* **74** (4), 46–51.

KIM, H., KIM, J., WON, S. & LEE, C. 2021 Unsupervised deep learning for super-resolution reconstruction of turbulence. *J. Fluid Mech.* **910**, A29.

KIM, W.-W. & MENON, S. 1996 *A new dynamic one-equation subgrid-scale model for large eddy simulations. AIAA Paper* 1995-356.

KIM, D. & MOIN, P. 2020 Subgrid-scale capillary breakup model for liquid jet atomization. *Combust. Sci. Technol.* **192** (7), 1334–1357.

KOLMOGOROV, A.N. 1941 The local structure of turbulence in incompressible viscous fluid for very large Reynolds numbers. *Dokl. Akad. Nauk SSSR* **30**, 299–303.

KUMAR, S., QUAN, H. & EYINK, G.L. 2021 Onsager approach to wall bounded turbulence. In *74th Annual Meeting of the American Physical Society Division of Fluid Dynamics*, vol. 66, issue 17, M04.00008. American Physical Society.

LABOURASSE, E., LACANETTE, D., TOUTANT, A., LUBIN, P., VINCENT, S., LEBAIGUE, O., CALTAGIRONE, J.P. & SAGAUT, P. 2007 Towards large eddy simulation of isothermal two-phase flows: governing equations and a priori tests. *Intl J. Multiphase Flow* **33** (1), 1–39.

LAKEHAL, D. 2018 Status and future developments of large-eddy simulation of turbulent multi-fluid flows (LEIS and LESS). *Intl J. Multiphase Flow* **104**, 322–337.

LANGFORD, J.A. & MOSER, R.D. 1999 Optimal LES formulations for isotropic turbulence. *J. Fluid Mech.* **398**, 321–346.

LANGFORD, J.A. & MOSER, R.D. 2001 Breakdown of continuity in large-eddy simulation. *Phys. Fluids* **13** (5), 1524–1527.

LARSSON, J., KAWAI, S., BODART, J. & BERMEJO-MORENO, I. 2016 Large eddy simulation with modeled wall-stress: recent progress and future directions. *Mech. Engng Rev.* **3** (1), 15–00418.

LEONARD, A. 1975 Energy cascade in large-eddy simulations of turbulent fluid flows. In *Turbulent Diffusion in Environmental Pollution* (ed. F.N. Frenkiel & R.E. Munn), Advances in Geophysics, vol. 18, pp. 237–248. Elsevier.

LEONARD, A. 2016 *Large-Eddy Simulation of the Navier–Stokes Equations: Deconvolution, Particle Methods, and Super-Resolution*, pp. 1–16. World Scientific.

LILLY, D.K. 1992 A proposed modification of the germano subgrid-scale closure method. *Phys. Fluids* **4** (3), 633–635.

LIU, B., TANG, J., HUANG, H. & LU, X.-Y. 2020 Deep learning methods for super-resolution reconstruction of turbulent flows. *Phys. Fluids* **32** (2), 025105.

LUND, T.S. & ROGERS, M.M. 1994 An improved measure of strain state probability in turbulent flows an improved measure of strain state probability in turbulent flows. *Phys. Fluids* **6**, 1838–1847.

MAULIK, R. & SAN, O. 2017 A neural network approach for the blind deconvolution of turbulent flows. *J. Fluid Mech.* **831**, 151–181.

MAXEY, M.R. & RILEY, J.J. 1983 Equation of motion for a small rigid sphere in a nonuniform flow. *Phys. Fluids* **26** (4), 883–889.

MCCASLIN, J.O. & DESJARDINS, O. 2014 Theoretical and computational modeling of turbulence / interface interactions. In *Center for Turbulence Research Proceedings of the Summer Program 2014*, pp. 79–88.

MENEVEAU, C., LUND, T.S. & CABOT, W.H. 1996 A lagrangian dynamic subgrid-scale model of turbulence. *J. Fluid Mech.* **319**, 353–385.
MILANO, M. & KOUMOUTSAKOS, P. 2002 Neural network modeling for near wall turbulent flow. *J. Comput. Phys.* **182** (1), 1–26.
MOCKETT, C., FUCHS, M. & THIELE, F. 2012 Progress in DES for wall-modelled LES of complex internal flows. *Comput. Fluids* **65**, 44–55.
MOIN, P., SQUIRES, K., CABOT, W. & LEE, S. 1991 A dynamic subgrid-scale model for compressible turbulence and scalar transport. *Phys. Fluids* **3** (11), 2746–2757.
MONIN, A.S. & YAGLOM, A.M. 1975 *Statistical Fluid Mechanics: Mechanics of Turbulence*, vol. II. Dover Publications.
MOREAU, A., TEYTAUD, O. & BERTOGLIO, J.P. 2006 Optimal estimation for large-eddy simulation of turbulence and application to the analysis of subgrid models. *Phys. Fluids* **18** (10), 105101.
MOSER, R.D., HAERING, S.W. & YALLA, G.R. 2021 Statistical properties of subgrid-scale turbulence models. *Annu. Rev. Fluid Mech.* **53** (1), 255–286.
PARK, J. & CHOI, H. 2021 Toward neural-network-based large eddy simulation: application to turbulent channel flow. *J. Fluid Mech.* **914**, A16.
PATTERSON, G.S. & ORSZAG, S.A. 1971 Spectral calculations of isotropic turbulence: efficient removal of aliasing interactions. *Phys. Fluids* **14** (11), 2538–2541.
PIOMELLI, U. & BALARAS, E. 2002 Wall-layer models for large-eddy simluations. *Annu. Rev. Fluid Mech.* **34** (1), 349–374.
POPE, S.B. 2000 *Turbulent Flows*. Cambridge University Press.
POPE, S.B. 2010 Self-conditioned fields for large-eddy simulations of turbulent flows. *J. Fluid Mech.* **652**, 139–169.
PORTWOOD, G.D., NADIGA, B.T., SAENZ, J.A. & LIVESCU, D. 2021 Interpreting neural network models of residual scalar flux. *J. Fluid Mech.* **907**, A23.
PRAKASH, A., JANSEN, K.E. & EVANS, J.A. 2021 Invariant data-driven subgrid stress modeling in the strain-rate eigenframe for large eddy simulation. arXiv:2106.13410.
ROZEMA, W., BAE, H.J., MOIN, P. & VERSTAPPEN, R. 2015 Minimum-dissipation models for large-eddy simulation. *Phys. Fluids* **27** (8), 085107.
SAGAUT, P. 2006 *Large Eddy Simulation for Incompressible Flows: An Introduction*. Springer.
SAGAUT, P. & GERMANO, M. 2005 On the filtering paradigm for LES of flows with discontinuities. *J. Turbul.* **6** (23), 1–9.
SARGHINI, F., DE FELICE, G. & SANTINI, S. 2003 Neural networks based subgrid scale modeling in large eddy simulations. *Comput. Fluids* **32** (1), 97–108.
SCOTTI, A. & MENEVEAU, C. 1999 A fractal model for large eddy simulation of turbulent flow. *Phys.* D **127** (3-4), 198–232.
SCOTTI, A., MENEVEAU, C. & LILLY, D.K. 1993 Generalized Smagorinsky model for anisotropic grids. *Phys. Fluids* A **5**, 2306–2308.
SIRIGNANO, J., MACART, J.F. & FREUND, J.B. 2020 DPM: A deep learning PDE augmentation method with application to large-eddy simulation. *J. Comput. Phys.* **423**, 109811.
SPALART, P.R. 2009 Detached-eddy simulation. *Annu. Rev. Fluid Mech.* **41** (1), 181–202.
STOFFER, R., VAN LEEUWEN, C.M., PODAREANU, D., CODREANU, V., VEERMAN, M.A., JANSSENS, M., HARTOGENSIS, O.K. & VAN HEERWAARDEN, C.C. 2021 Development of a large-eddy simulation subgrid model based on artificial neural networks: a case study of turbulent channel flow. *Geosci. Model Develop.* **14** (6), 3769–3788.
STOLZ, S. & ADAMS, N.A. 1999 An approximate deconvolution procedure for large-eddy simulation. *Phys. Fluids* **11** (7), 1699–1701.
TENNEKES, H. & LUMLEY, J.L. 1972 *A First Course in Turbulence*. MIT Press.
TOUTANT, A., CHANDESRIS, M., JAMET, D. & LEBAIGUE, O. 2009 Jump conditions for filtered quantities at an under-resolved discontinuous interface. Part 1: theoretical development. *Intl J. Multiphase Flow* **35** (12), 1100–1118.
TRYGGVASON, G. & LU, J. 2020 Direct numerical simulations of multiphase flows: opportunities and challenges. *AIP Conf. Proc.* **2293** (1), 030002.
VERSTAPPEN, R. 2011 When does eddy viscosity damp subfilter scales sufficiently? *J. Sci. Comput.* **49** (1), 94–110.
VOLLANT, A., BALARAC, G. & CORRE, C. 2017 Subgrid-scale scalar flux modelling based on optimal estimation theory and machine-learning procedures. *J. Turbul.* **18** (9), 854–878.
VREMAN, A.W. 2004 An eddy-viscosity subgrid-scale model for turbulent shear flow: algebraic theory and applications. *Phys. Fluids* **16** (10), 3670–3681.

VREMAN, B., GEURTS, B. & KUERTEN, H. 1994 On the formulation of the dynamic mixed subgrid-scale model. *Phys. Fluids* **6** (12), 4057–4059.

WANG, Z., LUO, K., LI, D., TAN, J. & FAN, J. 2018 Investigations of data-driven closure for subgrid-scale stress in large-eddy simulation. *Phys. Fluids* **30** (12), 125101.

WANG, Y., YUAN, Z., XIE, C. & WANG, J. 2021 Artificial neural network-based spatial gradient models for large-eddy simulation of turbulence. *AIP Adv.* **11** (5), 055216.

WANG, Q., ZHAO, X. & IHME, M. 2019 A regularized deconvolution model for sub-grid dispersion in large eddy simulation of turbulent spray flames. *Combust. Flame* **207**, 89–100.

XIE, C., WANG, J. & WEINAN, E. 2020*a* Modeling subgrid-scale forces by spatial artificial neural networks in large eddy simulation of turbulence. *Phys. Rev. Fluids* **5**, 054606.

XIE, C., YUAN, Z. & WANG, J. 2020*b* Artificial neural network-based nonlinear algebraic models for large eddy simulation of turbulence. *Phys. Fluids* **32** (11), 115101.

YALLA, G.R., OLIVER, T.A., HAERING, S.W., ENGQUIST, B. & MOSER, R.D. 2021 Effects of resolution inhomogeneity in large-eddy simulation. *Phys. Rev. Fluids* **6**, 074604.

YANG, X.I.A., ZAFAR, S., WANG, J.-X. & XIAO, H. 2019 Predictive large-eddy-simulation wall modeling via physics-informed neural networks. *Phys. Rev. Fluids* **4**, 034602.

YUAN, Z., XIE, C. & WANG, J. 2020 Deconvolutional artificial neural network models for large eddy simulation of turbulence. *Phys. Fluids* **32** (11), 115106.

ZHOU, Z., HE, G., WANG, S. & JIN, G. 2019 Subgrid-scale model for large-eddy simulation of isotropic turbulent flows using an artificial neural network. *Comput. Fluids* **195**, 104319.